A Simulation of the Wangara Atmospheric Boundary Layer Data

TETSUJI YAMADA AND GEORGE MELLOR

Geophysical Fluid Dynamics Program,[1] Princeton University, Princeton, N. J. 08540

(Manuscript received 5 May 1975, in revised form 25 August 1975)

ABSTRACT

Previously, the authors have studied a hierarchy of turbulent boundary layer models, all based on the same closure assumptions for the triple turbulence moments. The models differ in complexity by virtue of a systematic process of neglecting certain of the tendency and diffusion terms in the dynamic equations for the turbulent moments. Based on this work a Level 3 model was selected as one which apparently sacrificed little predictive accuracy, but which afforded considerable numerical simplification relative to the more complex Level 4 model.

An earlier paper had demonstrated that the model produced similarity solutions in near agreement with surface, constant flux data. In this paper, simulations from the Level 3 model are compared with two days of Wangara atmospheric boundary layer data (Clarke *et al.*, 1971). In this comparison, there is an easily identified error introduced by our inability to include advection of momentum in the calculation since these terms were not measured. Otherwise, the calculated results and the observational data appear to be in close agreement.

1. Introduction

The usual strategy in modeling turbulence utilizes eddy coefficient or mixing length theory. On this basis, numerical simulations of the diurnally varying planetary boundary layer have been discussed by a number of investigators including Estoque (1963), Sasamori (1970), Yamamoto *et al.* (1973) and Clarke (1974). Similar models emphasizing the nocturnal low-level jet have been reported by Buajitti and Blackadar (1957), Krishna (1968), Paegle and Rasch (1973) and Wipperman (1973). Although these eddy coefficient models have realistically simulated certain features observed in the diurnally varying planetary boundary layer, expressions for the eddy coefficient are chosen rather arbitrarily.

Deardorff (1974a,b) has developed a sophisticated, unsteady, three-dimensional numerical model wherein a portion of the turbulence is explicitly calculated and only subgrid-scale turbulence need be modeled; turbulence-moment transport equations requiring closure assumptions are utilized. However, Deardorff's model requires small resolution in all three dimensions and time and therefore requires a very large amount of computer time. A simplified two-dimensional version similar to Deardorff's approach was adopted by Orlanski *et al.* (1974).

In contrast to subgrid-scale closure, ensemble mean closure—wherein the turbulence moments are dependent variables—is a term we apply to the methods described by Donaldson (1973), Mellor (1973) and Lewellen *et al.* (1974). Wyngaard and Coté (1974), utilizing a simplified version of the turbulence closure model of Lumley and Kanjeh-Nouri (1974), claimed that their closure model could reproduce fairly well the results of the numerical simulation by Deardorff and, of course, with relatively small computation times.

The paper by Mellor (1973) first described the present model and related the necessary empirical constants to turbulence properties of simple neutral flow experiments. The model immediately produced similarity solutions in near agreement with data in the surface, constant-flux layer. Mellor and Yamada (1974) provided an analysis which systematically simplified the full closure model, termed a Level 4 model, which consists of at least ten differential equations for turbulence moments. A derived, intermediate Level 3 model requires solution of only two out of the ten differential equations (equations for turbulent kinetic energy and temperature variance), and reproduced practically the same results as obtained by the Level 4 model in a numerical experiment whereby a simulated atmospheric boundary layer was subject to a diurnally varying surface temperature. The Level 2 model reduces the entire turbulence model to algebra and can be cast in a traditional eddy coefficient format modified by derived Richardson-number-dependent functions.

We utilize the Level 3 model exclusively in the present investigation whose object is to give a full description of the numerical procedure and to present a detailed discussion of the results in comparison with observations from the Wangara experiment (Clarke *et al.*, 1971) for a period of 48 h from Days 33 through 35.

[1] Support provided through Geophysical Fluid Dynamics Laboratory/NOAA, under Grant 04-3-022-33.

2. The model

a. Governing equations

We define the virtual temperature

$$\tilde{T}_v \equiv (1+0.61\tilde{R})\tilde{T}, \tag{1}$$

where $\tilde{T}$ is the absolute temperature and $\tilde{R}$ the mixing ratio of water vapor. We also define a potential temperature

$$\tilde{\Theta} \equiv \tilde{T} + \gamma_d z \tag{2a}$$

and a virtual potential temperature

$$\tilde{\Theta}_v \equiv (1+0.61\tilde{R})\tilde{\Theta}, \tag{2b}$$

where γ_d is the dry adiabatic lapse rate [10 K (1000 m)$^{-1}$]. In the above, the tilde refers to instantaneous values whereas below, the tilde will be removed to indicate mean quantities. Within the range of scales to be studied, the Boussinesq approximation is permissable and is incorporated in the following analysis. The mean equations of motion which we plan to solve are

$$\frac{\partial U}{\partial t} - fV + \frac{\partial P}{\partial x} = \frac{\partial}{\partial z}(-\overline{uw}), \tag{3}$$

$$\frac{\partial V}{\partial t} + fU + \frac{\partial P}{\partial y} = \frac{\partial}{\partial z}(-\overline{vw}), \tag{4}$$

$$\frac{\partial \Theta_v}{\partial t} + U\frac{\partial \Theta_v}{\partial x} + V\frac{\partial \Theta_v}{\partial y} + W\frac{\partial \Theta_v}{\partial z} = \frac{\partial}{\partial z}(-\overline{w\theta_v}) + \sigma_r, \tag{5}$$

$$\frac{\partial R}{\partial t} = \frac{\partial}{\partial z}(-\overline{wr}), \tag{6}$$

where U, V, W, P, $\tilde{\Theta}_v$, R are the mean velocities in the x (eastward), y (northward), z (vertical) directions, kinematic pressure, virtual potential temperature, and mixing ratio of water vapor; and f is the Coriolis parameter whose numerical value is -0.826×10^{-4} s^{-1} at Hay, Australia (34°30′S, 144°56′E). The period of intertial oscillations is therefore ~21.1 h.

The turbulent moments of stress, heat and water vapor fluxes are $-\overline{uw}$, $-\overline{vw}$, $-\overline{w\theta_v}$, $-\overline{wr}$, respectively; and σ_r is the flux divergence of longwave radiation which has a perceptible influence on our calculated results. A simplified radiation model (based on fixed water vapor) has been supplied to us by Dr. Stephen Fels of the Geophysical Fluid Dynamics Laboratory. Water vapor condensation or evaporation has not been included in the present model. It is our intention to use the observed values for W in (5) as will be discussed in Section 4.

In the above equations it will be noted that temperature advection has been included since the necessary gradient terms can be estimated from the data set; on the other hand, velocity and water vapor advections must be excluded. One might hope that, in the case of velocity, the Coriolis terms would dominate the advective terms (we will see direct evidence that this hope is not entirely realized). On the other hand, neglect of water vapor advection is liable to be serious since only the tendency term remains to balance the flux divergence. Fortunately, the velocity and virtual temperature fields are not dependent on water vapor. Therefore, discussion of the calculated results for water vapor has been relegated to the Appendix.

In the Wangara data set, pressure gradient data were provided in the form of geostrophic wind profiles defined according to

$$(U_g, V_g) \equiv \frac{1}{f}\left(-\frac{\partial P}{\partial y}, \frac{\partial P}{\partial x}\right), \tag{7a,b}$$

so that, with the help of the hydrostatic assumption (Hess, 1959, p. 193) we may also write

$$\left(\frac{\partial \Theta_v}{\partial x}, \frac{\partial \Theta_v}{\partial y}\right) \approx \frac{fT_v}{g}\left(\frac{\partial V_g}{\partial z}, -\frac{\partial U_g}{\partial z}\right). \tag{8a,b}$$

Thus Eqs. (3), (4) and (5) may be written

$$\frac{\partial U}{\partial t} = fV - fV_g + \frac{\partial}{\partial z}(-\overline{uw}), \tag{9}$$

$$\frac{\partial V}{\partial t} = -fU + fU_g + \frac{\partial}{\partial z}(-\overline{vw}), \tag{10}$$

$$\frac{\partial \Theta_v}{\partial t} = \frac{\partial}{\partial z}(-\overline{w\theta_v}) + \frac{fT_v}{g}\left(V\frac{\partial U_g}{\partial z} - U\frac{\partial V_g}{\partial z}\right) - W\frac{\partial \Theta_v}{\partial z} + \sigma_r. \tag{11}$$

To the turbulence model described by Mellor and Yamada (1974), henceforth referred to as paper A, we have added the moment equations for water vapor and assumed the closure assumptions to be identical to those for potential temperature (see the Appendix for details). The resultant Level 3 model simplified for boundary layers requires the solution of differential equations for q^2, $\overline{\theta_v^2}$, $\overline{r^2}$ and $\overline{\theta_v r}$:

$$\frac{\partial}{\partial t}\left(\frac{q^2}{2}\right) - \frac{\partial}{\partial z}\left[\frac{5}{3}\lambda_1 q\frac{\partial}{\partial z}\left(\frac{q^2}{2}\right)\right] = -\overline{uw}\frac{\partial U}{\partial z} - \overline{vw}\frac{\partial V}{\partial z} + \beta g\overline{w\theta_v} - \frac{q^3}{\Lambda_1} \tag{12}$$

$$\frac{\partial}{\partial t}\left(\frac{\overline{\theta_v^2}}{2}\right) - \frac{\partial}{\partial z}\left[\lambda_3 q\frac{\partial}{\partial z}\left(\frac{\overline{\theta_v^2}}{2}\right)\right] = -\overline{w\theta_v}\frac{\partial \Theta_v}{\partial z} - q\frac{\overline{\theta_v^2}}{\Lambda_2} \tag{13}$$

$$\frac{\partial}{\partial t}\left(\frac{\overline{r^2}}{2}\right)-\frac{\partial}{\partial z}\left[\lambda_3 q\frac{\partial}{\partial z}\left(\frac{\overline{r^2}}{2}\right)\right]=-\overline{wr}\frac{\partial R}{\partial z}-q\frac{\overline{r^2}}{\Lambda_2} \tag{14}$$

$$\frac{\partial}{\partial t}(\overline{\theta_v r})-\frac{\partial}{\partial z}\left[\lambda_2 q\frac{\partial}{\partial z}(\overline{\theta_v r})\right]=-\overline{w\theta_v}\frac{\partial R}{\partial z}-\overline{wr}\frac{\partial \Theta_v}{\partial z}-\frac{2q}{\Lambda_2}\overline{\theta_v r}. \tag{15}$$

Once q^2, $\overline{\theta_v^2}$, $\overline{r^2}$ and $\overline{\theta_v r}$ have been determined, paper A provides equations for the components of the Reynold stress, heat flux and vapor flux:

$$\begin{pmatrix}\overline{u^2}\\ \overline{v^2}\\ \overline{w^2}\end{pmatrix}=\frac{q^2}{3}\begin{pmatrix}1\\1\\1\end{pmatrix}+\frac{l_1}{q}\begin{pmatrix}4P_{xx}-2P_{yy}-2\beta g\overline{w\theta_v}\\ -2P_{xx}+4P_{yy}-2\beta g\overline{w\theta_v}\\ -2P_{xx}-2P_{yy}+4\beta g\overline{w\theta_v}\end{pmatrix}-\frac{l_1}{q}\mathfrak{D}_1 q^2\begin{pmatrix}\frac{2}{3}\\ \frac{2}{3}\\ -\frac{4}{3}\end{pmatrix} \tag{16a,b,c}$$

$$-\begin{pmatrix}\overline{uv}\\ \overline{uw}\\ \overline{vw}\end{pmatrix}=3\frac{l_1}{q}\begin{pmatrix}P_{yx}+P_{xy}\\ (\overline{w^2}-cq^2)\dfrac{\partial U}{\partial z}-\beta g\overline{u\theta_v}\\ (\overline{w^2}-cq^2)\dfrac{\partial V}{\partial z}-\beta g\overline{v\theta_v}\end{pmatrix} \tag{17a,b,c}$$

$$-\begin{pmatrix}\overline{u\theta_v}\\ \overline{v\theta_v}\\ \overline{w\theta_v}\end{pmatrix}=3\frac{l_2}{q}\begin{pmatrix}\overline{uw}\dfrac{\partial \Theta_v}{\partial z}+\overline{w\theta_v}\dfrac{\partial U}{\partial z}\\ \overline{vw}\dfrac{\partial \Theta_v}{\partial z}+\overline{w\theta_v}\dfrac{\partial V}{\partial z}\\ \overline{w^2}\dfrac{\partial \Theta_v}{\partial z}-\beta g\overline{\theta_v^2}\end{pmatrix} \tag{18a,b,c}$$

$$-\begin{pmatrix}\overline{ur}\\ \overline{vr}\\ \overline{wr}\end{pmatrix}=3\frac{l_2}{q}\begin{pmatrix}\overline{uw}\dfrac{\partial R}{\partial z}+\overline{wr}\dfrac{\partial U}{\partial z}\\ \overline{vw}\dfrac{\partial R}{\partial z}+\overline{wr}\dfrac{\partial V}{\partial z}\\ \overline{w^2}\dfrac{\partial R}{\partial z}-\beta g\overline{\theta_v r}\end{pmatrix}. \tag{19a,b,c}$$

Here

$$P_{ij}\equiv-\overline{wu_i}\frac{\partial U_j}{\partial z},$$

$$\mathfrak{D}_1(q^2)\equiv\frac{\partial}{\partial z}\left[q\lambda_1\frac{\partial}{\partial z}(q^2)\right].$$

b. Algebraic reduction

In paper A it was shown that the Reynolds stress and turbulent heat flux equations can be simplified further. Thus, after considerable algebraic manipulation, Eqs. (16)–(18) reduced to

$$(-\overline{uw},\ -\overline{vw})=K_M\left(\frac{\partial U}{\partial z},\frac{\partial V}{\partial z}\right), \tag{20a,b}$$

$$-\overline{w\theta_v}=K_H'\frac{\partial \Theta_v}{\partial z}-\gamma_c, \tag{21}$$

where

$$K_M\equiv A_1 l\Big[(1-3c)q^5+3q^2\mathfrak{D}_f-9\beta g A_2 l^2\{4A_1 cq^3+A_2(q^3+3\mathfrak{D}_f)\}\frac{\partial \Theta_v}{\partial z}+9(\beta g)^2 qA_2 l^2(4A_1+3A_2)\overline{\theta_v^2}\Big]$$
$$\div\Big[q^4+6A_1^2 l^2 q^2|\partial \mathbf{V}/\partial z|^2+3A_1A_2 l^2\times\Big\{7q^2-18A_1A_2 l^2|\partial \mathbf{V}/\partial z|^2+36A_1A_2 l^2(\beta g)\frac{\partial \Theta_v}{\partial z}\Big\}\beta g\frac{\partial \Theta_v}{\partial z}\Big], \tag{22a}$$

$$K_H'\equiv A_2 l[(q^3+3\mathfrak{D}_f)-6A_1 lK_M|\partial \mathbf{V}/\partial z|^2]\div\left(q^2+12A_1A_2 l^2\beta g\frac{\partial \Theta_v}{\partial z}\right), \tag{22b}$$

$$\gamma_c\equiv\frac{3A_2 lq\beta g\overline{\theta_v^2}}{\left(q^2+12A_1A_2 l^2\beta g\dfrac{\partial \Theta_v}{\partial z}\right)}, \tag{23a}$$

$$\mathfrak{D}_f\equiv\frac{4}{3}A_1 l\frac{\partial}{\partial z}\left(\lambda_1 q\frac{\partial q^2}{\partial z}\right), \tag{23b}$$

$$|\partial \mathbf{V}/\partial z|^2\equiv(\partial U/\partial z)^2+(\partial V/\partial z)^2. \tag{23c}$$

The advantages in defining eddy coefficients K_M and K_H' for momentum and heat (or water vapor) become clear from the following discussion. We first replace $-\overline{uw}$ in Eq. (9) and $-\overline{vw}$ in Eq. (10) by $K_M(\partial U/\partial z)$ and $K_M(\partial V/\partial z)$. Then a complex equation may be formed from (9) and (10) to obtain

$$\frac{\partial \hat{V}}{\partial t}=-if(\hat{V}-\hat{V}_g)+\frac{\partial}{\partial z}\left(K_M\frac{\partial \hat{V}}{\partial z}\right), \tag{24}$$

where $\hat{V}=U+iV$ and $\hat{V}_g\equiv U_g+iV_g$. In this form (24) can be solved by a complex implicit finite-difference

TABLE 1. Identification of the variable ϕ and the parameters P_1–P_4 in Eq. (26) corresponding to the prognostic equations for mean velocity, mean virtual potential temperature, turbulent energy and temperature variance.

	ϕ	P_1	P_2	P_3	P_4
Eq. (24)	$\hat{V}$	K_M	0	if	$if\hat{V}_g$
Eq. (25)	Θ_v	K_H'	W	0	$\frac{fT_v}{g}\left(V\frac{\partial U_g}{\partial z}-U\frac{\partial V_g}{\partial z}\right)+\sigma_r-\frac{\partial \gamma_c}{\partial z}$
Eq. (12)	$\frac{q^2}{2}$	$\frac{5}{3}q\lambda_1$	0	$\frac{q}{\Lambda_1}$	$-\overline{uw}\frac{\partial U}{\partial z}-\overline{vw}\frac{\partial V}{\partial z}+\beta g\overline{w\theta}$
Eq. (13)	$\frac{\overline{\theta^2}}{2}$	$q\lambda_3$	0	$\frac{q}{\Lambda_2}$	$-w\theta\frac{\partial \Theta_v}{\partial z}$

scheme. Similarly (11) can be rewritten as

$$\frac{\partial \Theta_v}{\partial t}=\frac{\partial}{\partial z}\left(K_H'\frac{\partial \Theta_v}{\partial z}\right)-\frac{\partial \gamma_c}{\partial z}-W\frac{\partial \Theta_v}{\partial z}+\frac{fT_v}{g}\left(V\frac{\partial U_g}{\partial z}-U\frac{\partial V_g}{\partial z}\right)+\sigma_r. \quad (25)$$

Consequently, all the equations to be solved can be reduced to a general expression given by

$$\frac{\partial \phi}{\partial t}=\frac{\partial}{\partial z}\left(P_1\frac{\partial \phi}{\partial z}\right)-P_2\frac{\partial \phi}{\partial z}-P_3\phi+P_4. \quad (26)$$

Table 1 identifies ϕ, P_1, P_2, P_3 and P_4 for Eqs. (24), (25), (12) and (13).

c. Turbulent length scale

As in paper A, all the length scales are assumed to be proportional to each other. In particular, the most important scales are

$$(l_1,l_2,\Lambda_1,\Lambda_2)=(A_1,A_2,B_1,B_2)l, \quad (27)$$

where

$$(A_1,A_2,B_1,B_2)=(0.78, 0.79, 15.0, 8.0).$$

Additionally we have set $C=0.056$ and $(\lambda_1,\lambda_3)=(0.23, 0.23)l$; calculated results are not overly sensitive to the latter three constants. The relation of these constants to simple properties of neutral turbulent flow data has been discussed by Mellor (1973).

An expression for l utilizing Blackadar's (1962) interpolation formula was proposed in paper A. Thus,

$$l=\frac{kz}{1+\frac{kz}{l_0}}, \quad l_0=\alpha\frac{\int_0^\infty qzdz}{\int_0^\infty qdz}, \quad (28a,b)$$

where $\alpha=0.10$ and k is the von Kármán constant; a value of 0.35 is assumed according to Businger *et al.* (1971). Thus, $l\sim kz$ as $z\to 0$ and $l\sim l_0$ as $z\to\infty$. This length scale prescription gave realistic simulations in paper A. In the absence of a more rationally conceived formulation, Eqs. (28a,b) are again adopted in the present paper. In Section 6 the sensitivity of the computed results with respect to the parameter α will be discussed.

d. The grid system and the finite-difference approximation

The finite-difference versions of Eqs. (9)–(15) yield the fact that the vertical increments generally appear in the combination $\Delta z/l$. Thus, since l is proportional to z near the surface but tends toward a constant away from the surface, computational accuracy is enhanced if we define a transformed coordinate ξ such that $\Delta\xi\propto$ constant $\equiv\Delta z/z$ for small z, whereas $\Delta\xi\propto$ constant $\equiv\Delta z$ for large z. Thus, we define

$$\xi=a_1z+a_2\ln(z/a_3). \quad (29)$$

For the present calculations we have chosen

$$a_1=0.0376\ \text{m}^{-1},\quad a_2=0.417 \text{ and } \quad a_3=z_0=0.01\ \text{m}.$$

Table 2 shows the 80-point distribution used in the present simulation. The differential equation (26) is transformed into the new coordinate system ξ through the relation (29) before it is discretized into its finite-difference equivalent. More specifically,

$$\frac{\partial \phi}{\partial z}=a\frac{\partial \phi}{\partial \xi},$$

TABLE 2. Relation between the transformed vertical coordinate and physical height. The total number of grid points is 80.

Grid ξ	Height z (m)	Grid ξ	Height z (m)
1	0.1	15	285.2
2	1.1	⋮	⋮
3	7.1	⋮	⋮
4	21.4	30	674.6
5	40.8	⋮	⋮
6	62.6	⋮	⋮
7	85.7	50	1200.1
8	109.6	⋮	⋮
9	134.0	⋮	⋮
10	158.7	80	199.23
⋮	⋮		

where

$$a\equiv\frac{d\xi}{dz}=a_1+\frac{a_2}{z}, \tag{30}$$

Using (30), a finite-difference expression for Eq. (26) (by Laasonen) is

$$\phi_j^{k+1}-\phi_j^k=\frac{a_j\delta t}{2(\delta\xi)^2}\left[\{(P_1a)_{j+1}^k+(P_1a)_j^k\}\phi_{j+1}^{k+1}\right.$$
$$-\{(P_1a)_{j+1}^k+2(P_1a)_j^k+(P_1a)_{j-1}^k\}\phi_j^{k+1}$$
$$\left.+\{(P_1a)_j^k+(P_1a)_{j-1}^k\}\phi_{j-1}^{k+1}\right]-\frac{a_jP_2^{k+1}\delta t}{2(\delta\xi)}\{\phi_{j+1}^{k+1}-\phi_{j-1}^{k+1}\}$$
$$-\delta t(P_3\phi_j^{k+1}-P_4^k). \tag{31}$$

The subscripts j and k represent the jth grid point from the surface and the kth time step. A constant value of 60 s for $\delta t\equiv t^{k+1}-t^k$ was used. A linear stability analysis with $P_1=$ constant (not included here) shows that the scheme given by Eq. (31) is unconditionally stable if P_3 is not negative. This is the case as seen from Table 1 for all the equations to be solved here. Eq. (31) is solved by the Gaussian elimination method (Richtmyer and Morton, 1967, p. 198) since this equation reduces to $\mathbf{A}\phi=\mathbf{B}$ where $\mathbf{A}$ is a tridiagonal matrix. The 2-day simulation required about 2.5 min CPU time on the IBM360/195 at the Geophysical Fluid Dynamics Laboratory at Princeton; however, this includes 30 contour line microfilm plots some of which are presented in this paper.

3. Initial and boundary conditions

The integration is started at 0900 on Day 33 (16 August 1967) of the Wangara field observation. This particular time is chosen partly to facilitate a direct comparison of results with those by Deardorff (1974) and by Wyngaard and Coté (1974). Initial values for U, V, $\tilde{\Theta}_v$ and R are the observed values. Fig. 1 shows

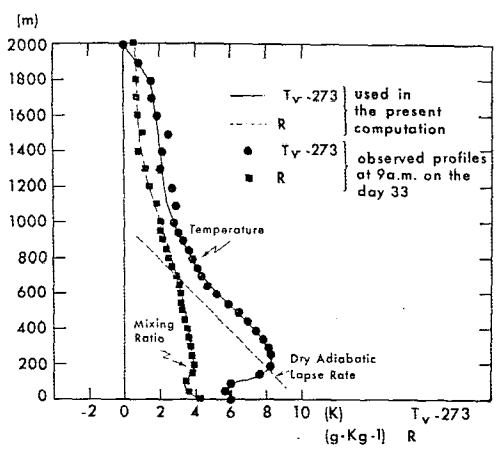

FIG. 1. Initial profiles for virtual temperature and water vapor mixing ratio.

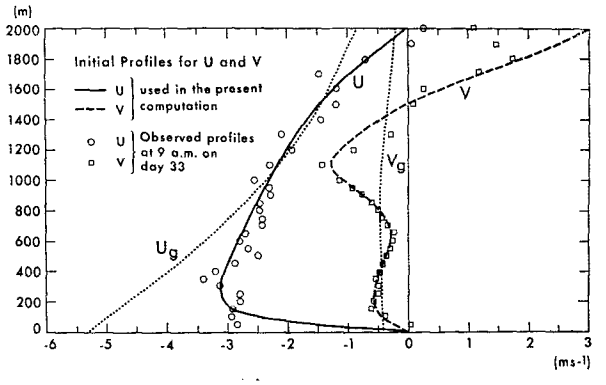

FIG. 2. Initial profiles for the mean wind components U and V. The geostrophic wind components (U_g,V_g) are also included.

the initial profiles for T_v and R which are obtained by drawing smoothed curves through the data points. Initial profiles for U and V are shown in Fig. 2. Near $z=2000$ m the V profile involves some temporal smoothing as well as spacial smoothing as discussed later in conjunction with Fig. 10. Initial values for the turbulence moments q^2 and $\overline{\theta_v^2}$ are generated by the model itself after a 1 h integration using guessed initial values for q^2 and $\overline{\theta_v^2}$. Then the mean values U, V, Θ_v and R are reinitialized to the 0900 values shown in Figs. 1 and 2. The computation is terminated when the model is integrated for 48 physical hours.

Close to the surface our model yields neutral flow relations; in particular,

$$(U,V)\sim(\cos\alpha,\sin\alpha)\frac{u_\tau}{k}\ln\frac{z}{z_0},\quad z\to 0, \tag{32a,b}$$

where

$$u_\tau\equiv\left[(-\overline{uw})^2+(-\overline{vw})^2\right]_{z=0}^{1/4},$$

and α is the angle of the surface stress vector. Similarly,

$$\Theta_v-\Theta_{v0}=\mathrm{Pr}_t\frac{H}{ku_\tau}\ln\frac{z}{z_{0t}},\quad z\to 0, \tag{33}$$

where

$$H=\left[-\overline{w\theta_v}\right]_{z=0}.$$

Note that Eqs. (32a,b) and (33) are means of introducing empirical roughness parameters such that (32a,b) and (33) yield real velocities and temperatures only when $z\gg z_0=O(z_{0t})^2$. The velocity roughness parameter z_0 and the thermal roughness parameter z_{0t} need not be equal. However, in the calculations discussed later, we have set $z_0=z_{0t}=1$ cm. The turbulent Prandtl number, $\mathrm{Pr}_t=0.74$, is related to the constants (A_1, A_2, B_1, B_2, C) as discussed by Mellor (1973).

[2] From p. 80 in Rotta (1962) one can estimate that the logarithmic behavior ceases to be valid in the range $0<z<5$–$10\ z_0$ for fully rough surfaces or $0<z<20\ \nu/u_\tau$ for smooth surfaces.

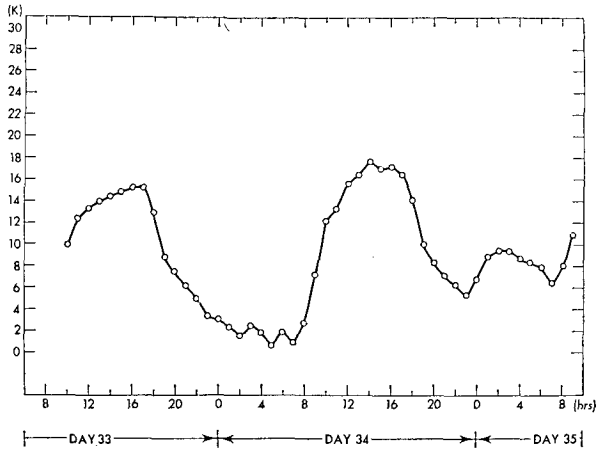

FIG. 3. Time variation of the observed virtual potential temperature at screen height (1.2 m) which is used as a lower boundary condition in the model.

The surface boundary conditions for q^2 and $\overline{\theta_v^2}$ determined in paper A are

$$q^2(0)=B_1^{\frac{2}{3}}u_\tau^2, \tag{34a}$$

$$\overline{\theta_v^2}(0)=\frac{H^2}{u_\tau^2}\frac{B_2}{B_1^{\frac{1}{3}}}\mathrm{Pr}_t. \tag{34b}$$

In particular, the ratio $q^2/u_\tau^2=B_1^{\frac{2}{3}}=6.10$ is a repeatedly observed surface value as discussed by Mellor (1973) whereas the constants appearing in (34b) related to measurements of turbulent velocity and temperature variance dissipation rates.

As discussed below, u_τ and H can be determined so that (32a,b), (33) and (34a,b) provide boundary conditions to the finite-difference forms of (3), (4), (5), (12) and (13), respectively. However, (32a,b) and (33) cannot be applied at $z=0$, but for the first points above the surface, $z_2>z_1>0$, (32a,b) yields

$$(U_1,V_1)=(U_2,V_2)\frac{\ln(z_1/z_0)}{\ln(z_2/z_0)}. \tag{35a,b}$$

This relation between two points provides a finite-difference boundary condition for velocity. The surface temperatures Θ_{vm} were actually measured at the "screen height" $z_m=1.2$ m which did not happen to correspond to a computational grid point. However, from (33) we can obtain

$$\Theta_{v2}=\Theta_{v3}\left[\frac{\ln(z_2/z_m)}{\ln(z_3/z_m)}\right]+\Theta_{vm}\left[1-\frac{\ln(z_2/z_m)}{\ln(z_3/z_m)}\right]. \tag{36}$$

Values at z_2 and z_3 are utilized rather than z_1 and z_2 since a numerical stability criterion requires that the factor in the first square bracket be less than unity. The measured values of Θ_{vm} are shown in Fig. 3. Once the velocity field has been solved for all grid points $z\geqslant z_1$, and the temperature field for all grid points $z\geqslant z_2$, the closest to the surface that $\overline{uw}$ and $\overline{vw}$ can be obtained from (17b,c) is at $z=z_2$, whereas the closest to the surface that $\overline{w\theta_v}$ can be obtained from (18c) is at $z=z_3$. To be consistent, we have then approximated the surface values of stress and heat flux to be constant in the region $z_3\geqslant z\geqslant 0$; u_τ and H are therefore determined from the Reynolds stress and heat flux at $z=z_3$.

At the upper boundary ($z=2000$ m)

$$q^2(h)=\overline{\theta_v^2}(h)=0. \tag{37a,b}$$

Formally, additional upper boundary conditions were

$$\frac{\partial U}{\partial z}=\frac{\partial V}{\partial z}=0, \tag{38}$$

$$\frac{\partial \Theta_v}{\partial z}=0.001\ \mathrm{K\ m^{-1}}. \tag{39}$$

However, the velocity field is decoupled from the upper boundary values since the computed Reynolds stresses were negligible there. If one inputs measured velocities at $z=2000$ m, a discontinuity is generated since, as discussed below, the measured and computed velocities differ by virtue of the neglect of advection in the latter. Similarly, the computed heat fluxes were negligible so that the computational equation is

$$\frac{\partial \Theta_v}{\partial t}+W\frac{\partial \Theta_v}{\partial z}=F(z,t),$$

where $F(z,t)$ are all the other terms in Eq. (11). To determine $\partial\Theta_v/\partial z$ from the measured values, Θ_v (2000 m,t), along with measured values of W, would be hazardous since W is of very marginal accuracy and, for example, an artifically unstable layer could be created at $z=2000$ m.

4. The geostrophic wind and the vertical wind

Aside from the fact that surface heat flux or surface temperature may be entered into the problem as boundary conditions, other input information that can be obtained from the data set includes the pressure gradient distribution (or geostrophic wind distribution) and the mean vertical wind.

The surface values of the geostrophic wind components U_g and V_g were estimated in two ways using (7a,b): from surface pressures read as hourly intervals at five closely spaced stations and from pressures interpolated from these five stations and 14 widely spaced, Bureau of Meteorology stations at 3 h intervals. Fig. 4 shows the surface geostrophic winds obtained by both methods. As seen from the figure the values obtained by the first method show considerable fluctuation since

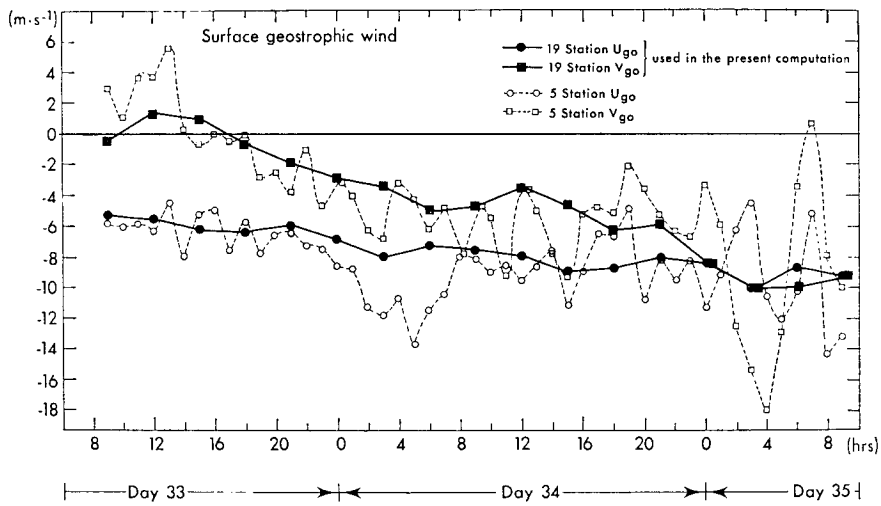

FIG. 4. Time variation of the observed surface geostrophic wind components (U_{g0}, V_{g0}). Values from the 19 stations (solid lines) are used in the computation.

the surface pressure difference between five stations (60 km) are comparable to the measuring error (~0.1 mb). In fact, it is reported that, in disturbed periods, oscillations of about 1 mb amplitude are common. Therefore the values obtained from the second method are utilized for the surface geostrophic winds U_{g0} and V_{g0}. The values between the measurements (3 h intervals) are linearly interpolated.

Thermal winds from the surface to 1 km height and from 1 to 2 km were estimated twice per day (0900 and 2100) from the Bureau of Meteorology synoptic radiosonde network. Table 3 summarizes the vertical shear of the geostrophic winds at 0900 and 2100 for Days 33 through 35. Parabolic profiles were fitted to these values so that the eastward geostrophic wind is given by

$$U_g(l,z)=\frac{(\Delta U_g)_2-(\Delta U_g)_1}{2\times10^6}z^2+\frac{3(\Delta U_g)_1-(\Delta U_g)_2}{2\times10^3}z+U_{g0}(l),$$

where $(\Delta U_g)_1$ and $(\Delta U_g)_2$ are the reported thermal winds differences from the surface to 1 km and from 1 to 2 km, respectively. The values for $(\Delta U_g)_1$ and $(\Delta U_g)_2$ at times between observations are linearly interpolated. The resultant geostrophic wind, U_g is shown in Fig. 5a. A similar result for V_g is shown in Fig. 5b.

TABLE 3. The observed thermal wind differences (m s^{-1}) at 0900 and 2100 from Days 33 through 35. The subscript 1 refers to the difference between the surface and 1 km whereas the subscript 2 refers to the difference between 1 km and 2 km.

	Day 33		Day 34		Day 35
	0900	2100	0900	2100	0900
$(\Delta U_g)_1$	2.98	2.81	1.87	1.91	1.70
$(\Delta V_g)_1$	−0.04	−0.67	0.59	1.30	1.21
$(\Delta U_g)_2$	1.49	1.32	1.04	−0.52	2.91
$(\Delta V_g)_2$	0.26	0.45	0.98	1.19	0.04

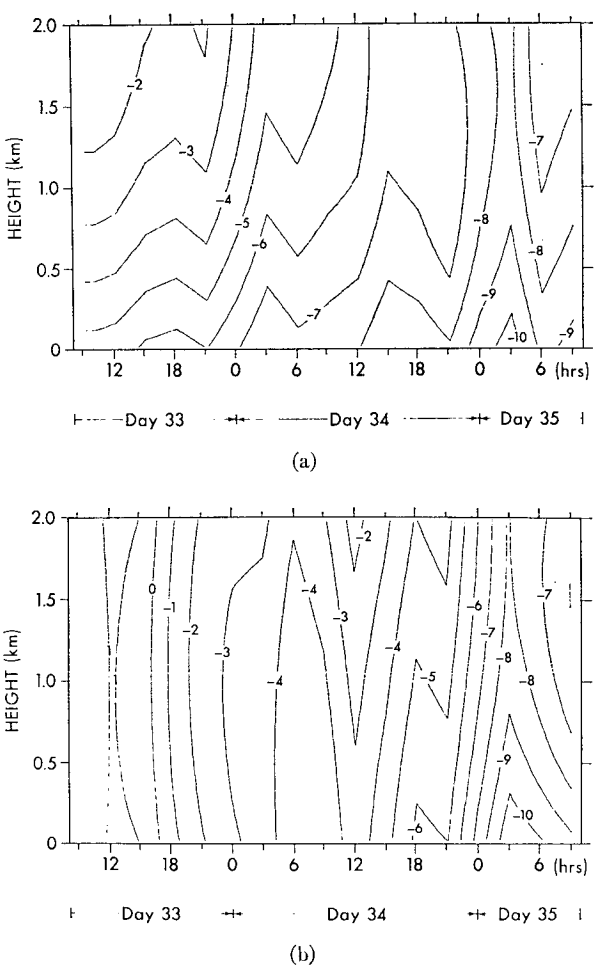

FIG. 5. Time and space variation of the eastward (a) and northward (b) geostrophic wind components (m s^{-1}) constructed from the observed surface geostrophic wind (Fig. 4) and observed thermal wind (see text for detail).

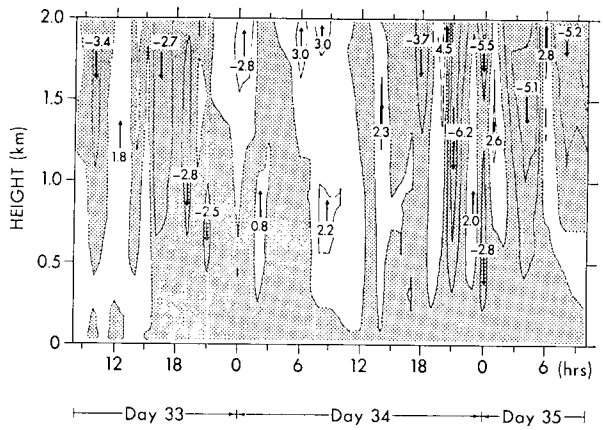

FIG. 6. Hourly profiles of the observed mean vertical wind (cm s^{-1}). The stippled regions indicate downward motion.

The effect of mean vertical wind on the structure of the planetary boundary layer has not been well studied. This is partly due to the difficulty in measuring W accurately. Furthermore, if the flow is horizontally homogeneous, the mean vertical wind should vanish, and although the Wangara field site was chosen so that horizontal homogeneity was supposedly well-satisfied, the data indicate relatively large values for the mean vertical wind, typically of the order of 2 cm s^{-1} during the period from Days 33 through 35 (see Fig. 6). The values for W were derived from the divergence equation and horizontal velocities on the corners of a 60 km square array. Therefore, the error in W is relatively large and estimated to be about 1.8 cm s^{-1} at 1000 m above the surface (Hess and Clarke, 1973). Nevertheless, we will include the observational vertical velocities in the equation for temperature and then later do a second calculation where the vertical velocity has been set equal to zero in order to assay the relative effects of this variable.

5. Results

The computed results can be divided into two categories: mean variables where there exist data for direct comparison and turbulence quantities where no data exist.[3]

[3] It is possible to compare with aircraft turbulence data collected by Telford and Warner (1964) and Lenschow (1970), for example, but agreement or lack of agreement would be purely circumstantial since the "boundary conditions" governing these data differ from those for the Wangara experiment. The afternoon temperature variance profile obtained by Telford and Warner does, in fact, agree very well with our calculations whereas the calculated dissipation profile differs considerably from that obtained by Lenschow. Dissipation profiles observed by Gamo *et al.* (1975) are similar in shape to our calculated profiles.

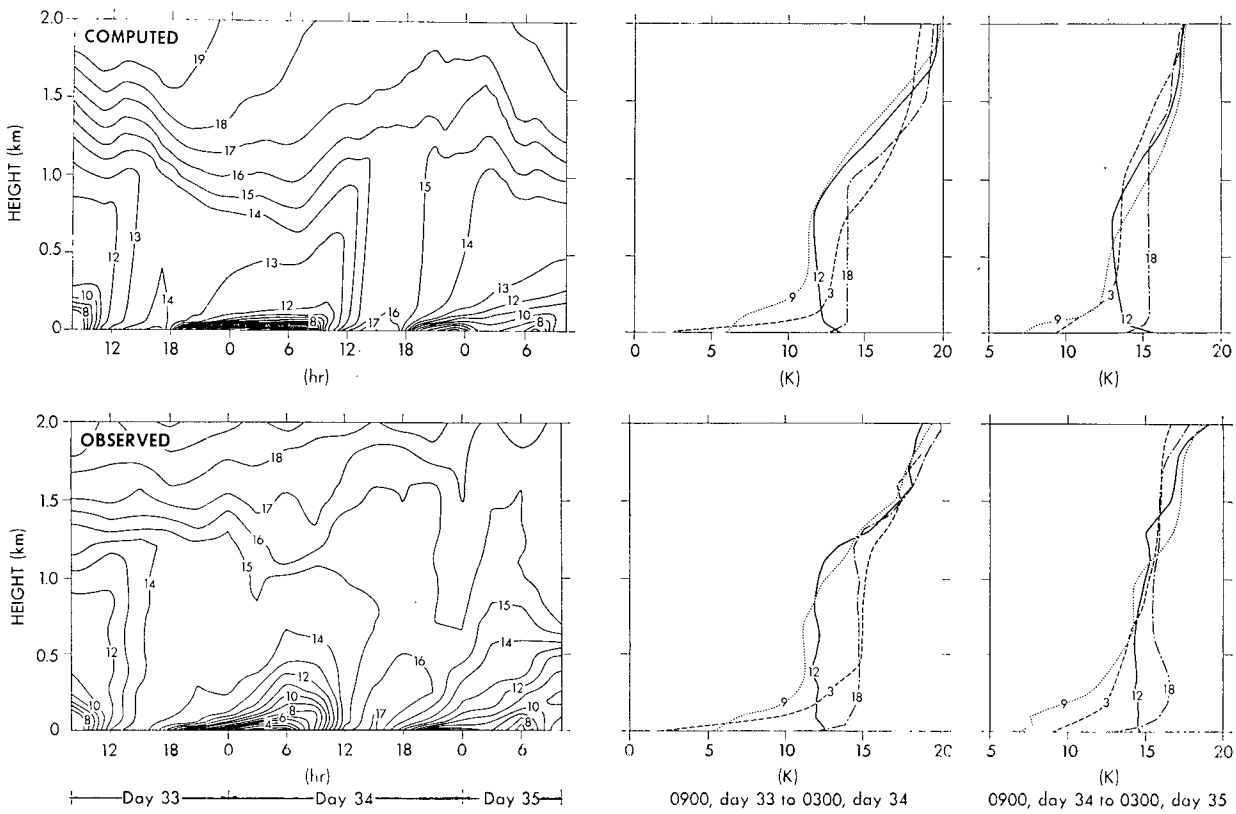

FIG. 7. Time and space variation of the computed and observed mean virtual potential temperature. Vertical profiles at various times are also included. The values on the contour lines ($\Theta_v - 273$) are in units of degrees K.

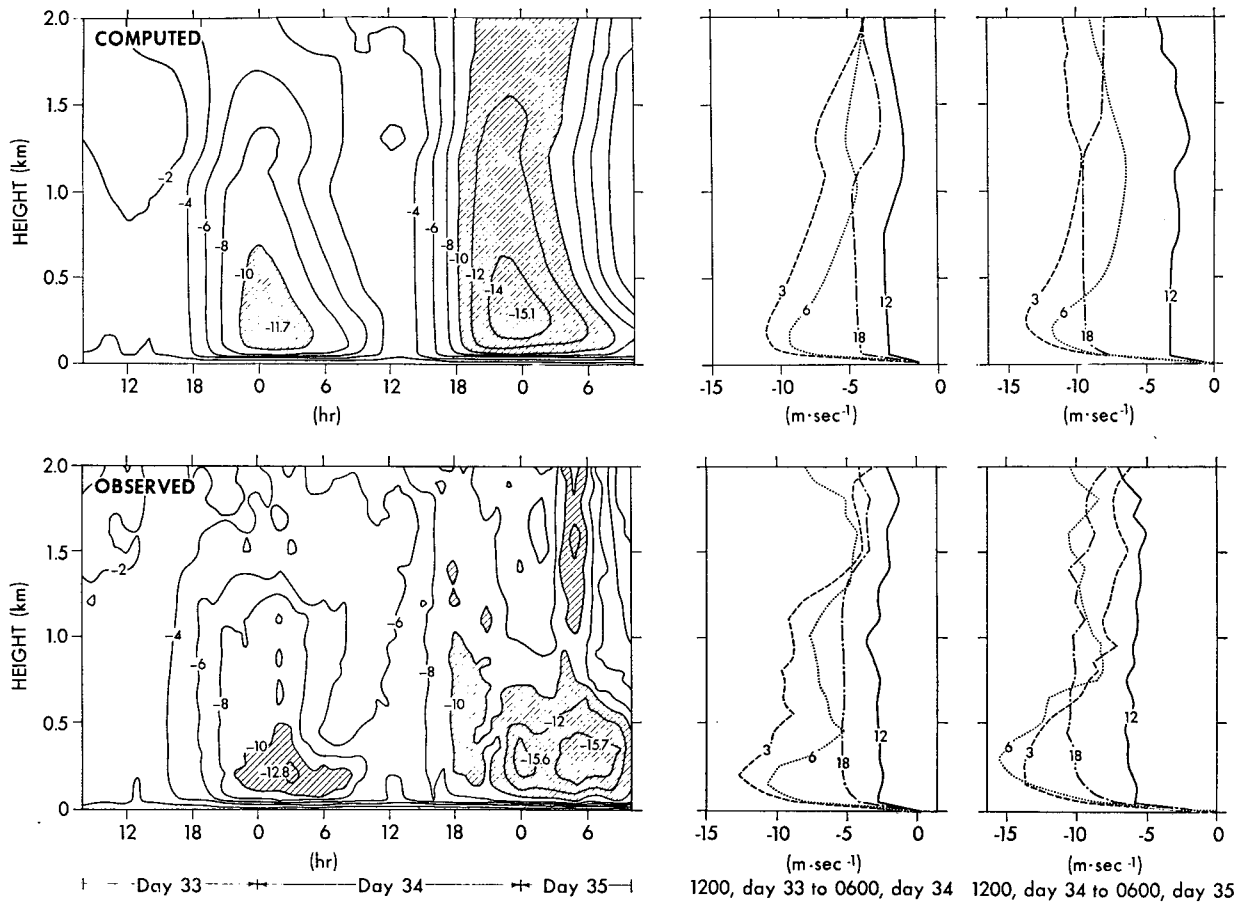

FIG. 8. Time and space variation of the eastward mean wind component U. The values on the contour line plots are in units of meters per second.

Nevertheless, the computed turbulence results, if accepted as reality, help explain the behavior of the mean quantities. Thus, while discussing the observed and computed mean variables, we will refer to the computed turbulence variables.

a. Mean variables

The mean temperatures and velocities are compared in the contour plots of Figs. 7, 8 and 9; typical daytime and nighttime profiles are included on the right sides of these figures.

In Fig. 7, during the daytime (0800 to 1800), a thin very unstable layer is observed between the surface and a well-mixed homogeneous layer above. The mixed layer is topped by a stable temperature inversion layer where, according to Fig. 11, the turbulence is negligible. Subsequently, during the nighttime (1800 to 0800) a ground-based temperature inversion layer develops whereas the mixed layer above retains a nearly constant virtual potential temperature. According to Fig. 11, the turbulence level in this layer during the nighttime is very low whereas, during the daytime, intense turbulence is observed in the same layer. At night, increased temperatures in the layer between 500 and 1500 m are due to large-scale subsidence (see Fig. 6) of the warm air above; this warming is reduced by radiation cooling, however. The computed virtual potential temperatures show reasonable agreements with those observed. Close examination of the results, though, reveal some discrepancies. For example, model temperatures in the mixed layer during the daytime are slightly lower than observed temperatures.

In Figs. 8 and 9, the daytime wind profiles are nearly constant in the mixed layer as a result of strong turbulence mixing. Right after sunset, the boundary layer becomes stable and the momentum flux is negligible (see Figs. 15 and 16). As explained by Blackadar (1957), low-level wind maxima or nocturnal jets can subsequently develop as a consequence of free inertial oscillations. Thus it may be approximately shown that the nocturnal jets that develop after 1800 in the region 1000 m$>z>0$ are simple solutions to (9) and (10) when $\partial(-\overline{uw})/\partial z=\partial(-\overline{vw})/\partial z=0$ using initial conditions at 1800 and the geostrophic velocities given in Figs. 5a and 5b. The fact that the computed wind maxima agree well with observations of two such events implies that

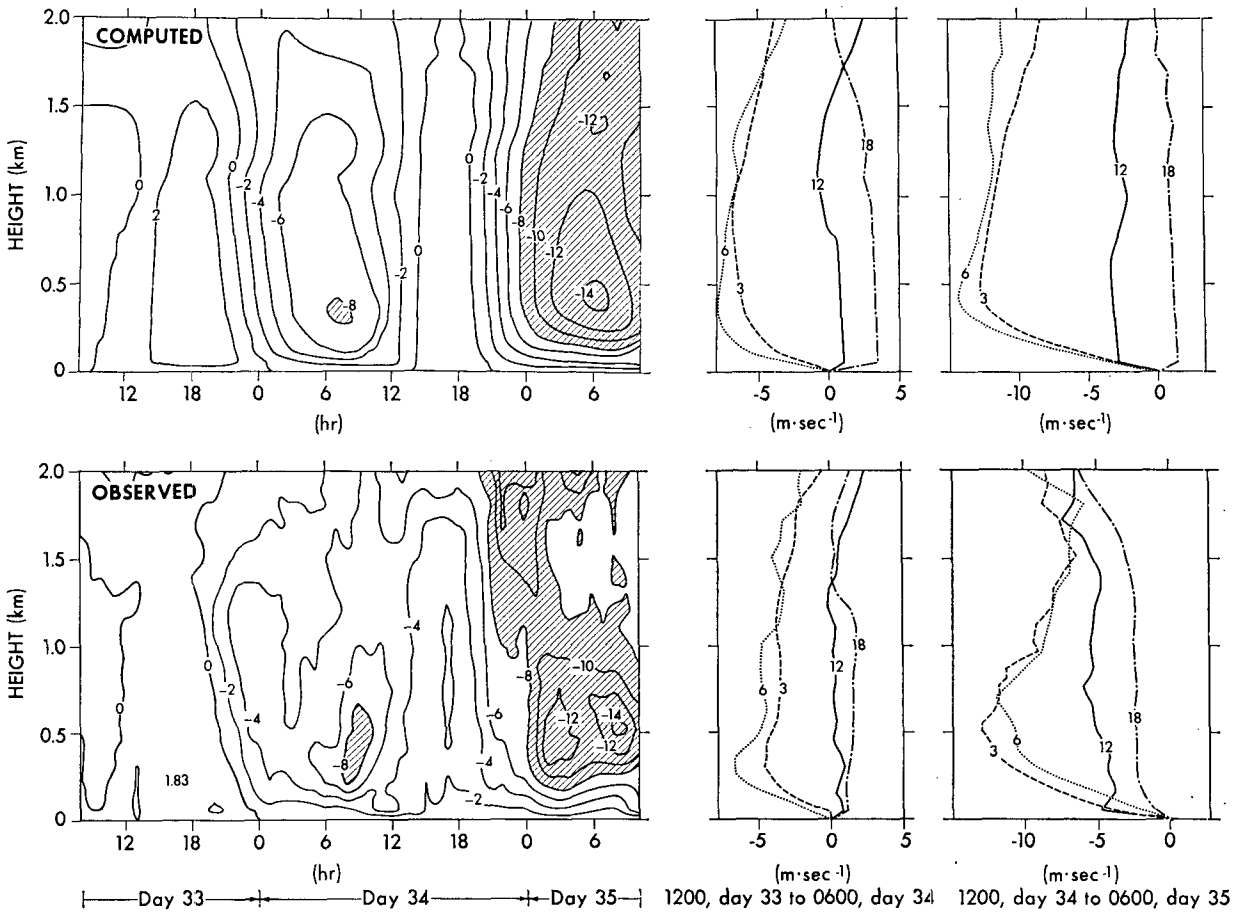

FIG. 9. As in Fig. 8 except for the northward mean wind component V.

we have correctly simulated the initial condition at $t \approx 1800$ and the subsequent vanishing of the Reynolds stresses.

In Fig. 10, we draw particular attention to the velocity and geostrophic wind at 2000 m. According to results discussed below (see Figs. 15 and 16) the momentum fluxes are negligible at this height. If this is accepted as reality, then any discrepancy between observed values and the strictly inertial motion computed from (24) with $\overline{uw}=\overline{vw}=0$ must be attributed to the neglect of

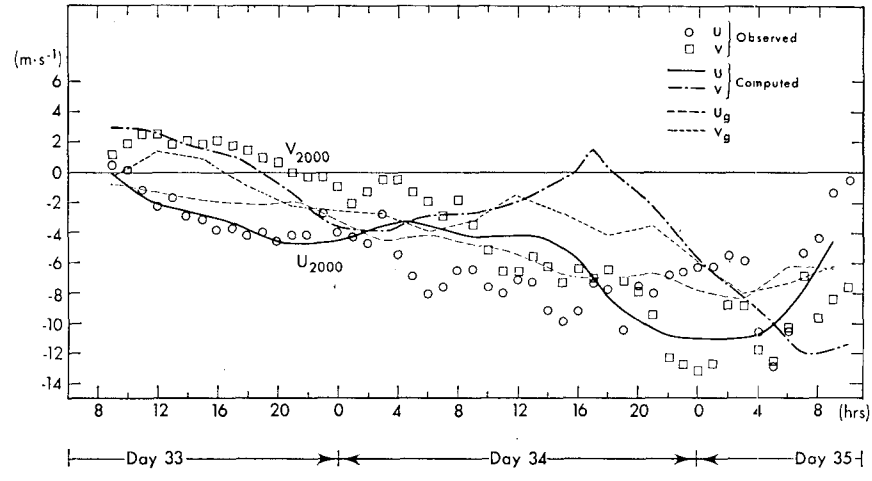

FIG. 10. Time variation of the computed and observed wind components at $z=2$ km as well as the geostrophic wind components at the same height.

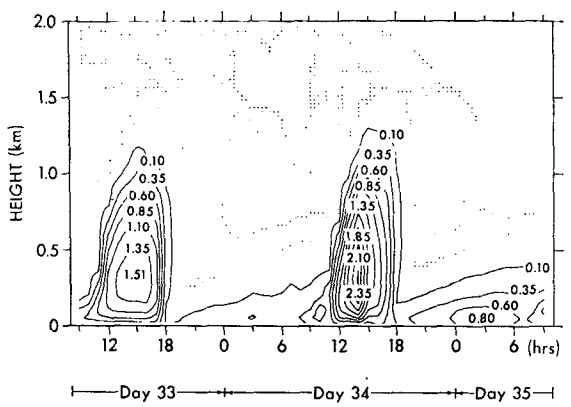

FIG. 11. Time and space variation of the computed q^2 (twice the turbulent kinetic energy, units $m^2\ s^{-2}$). The stippled areas indicate regions where $10^{-3}\ m^2\ s^{-2} < q^2 < 10^{-2}\ m^2\ s^{-2}$.

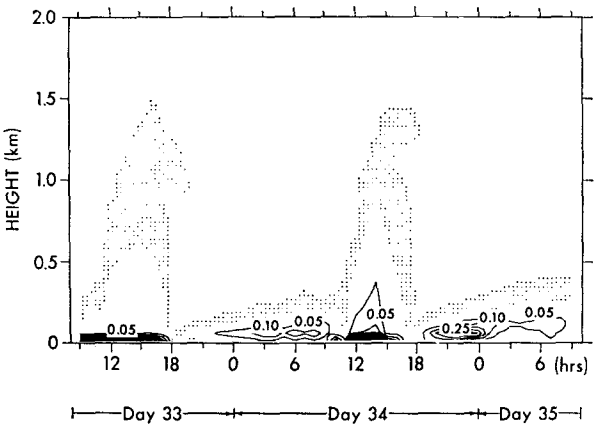

FIG. 13. Time and space variation of $\overline{\theta_v^2}$ (virtual potential temperature variance, units K^2). Maximum values at the surface are 0.79 and 1.9 K^2 at 1300 on Day 33 and 1400 on Day 34, respectively. The stippled area indicates regions where $0.001\ K^2 < \overline{\theta_v^2} < 0.01\ K^2$.

the advective terms. We believe it is this kind of error that is seen in Fig. 10, particularly during Day 34. Of course, this "error of omission" affects the entire mean velocity field as seen most strikingly on Day 34 in Figs. 8 and 9 for $z = 500$ m and upward.

b. *Turbulence variables*

Since the Wangara experiment was designed mainly for the measurements of the mean variables and certain turbulence fluxes near the surface layer, there is no

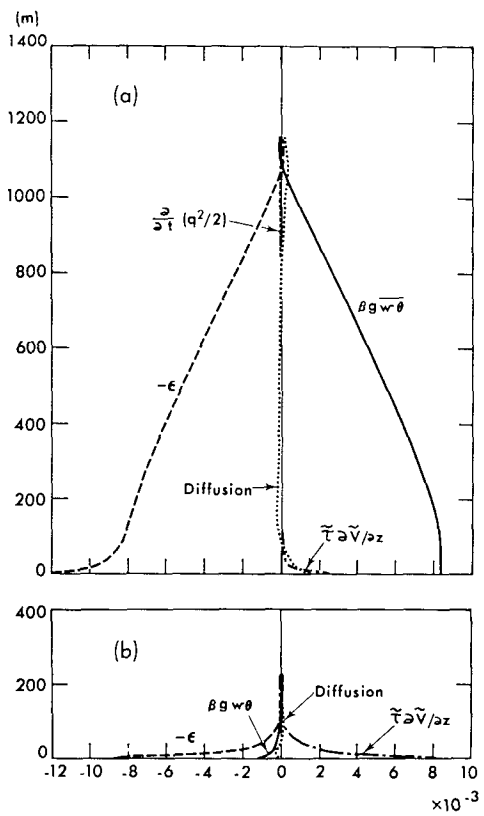

FIG. 12. Computed profiles of the terms in the turbulent kinetic energy equation (12), units $m^2\ s^{-3}$, at 1400 (a) and 1800 (b) on Day 34.

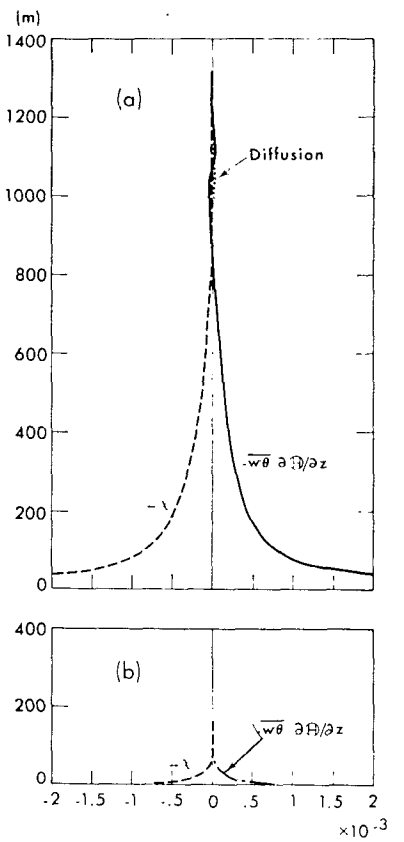

FIG. 14. Computed profiles of the terms in temperature variation equation (13), units $K^2\ s^{-1}$.

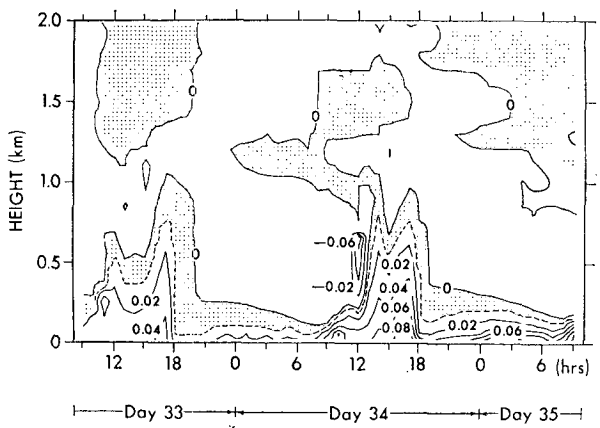

FIG. 15. Time and space variation of the computed Reynolds stress $\overline{uw}$, units $m^2 s^{-2}$. The stippled areas indicate regions where $\overline{uw}$ are positive but less than $10^{-2} m^2 s^{-2}$.

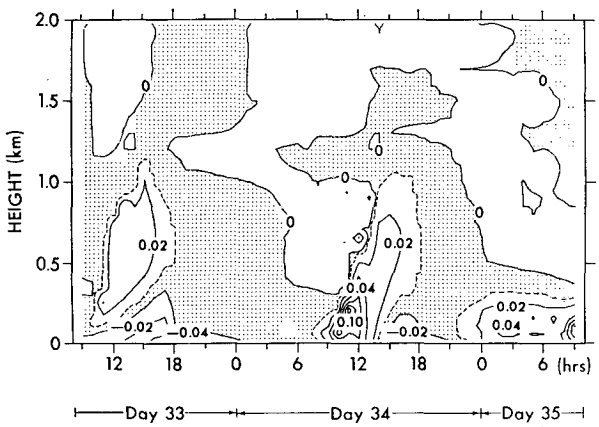

FIG. 16. Time and space variation of the computed Reynolds stress $\overline{vw}$.

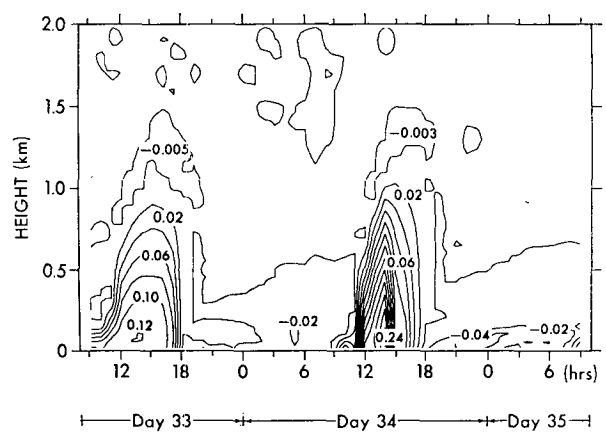

FIG. 17. Hourly profiles of the computed turbulent heat flux $\overline{w\theta_v}$, units m K s^{-1}.

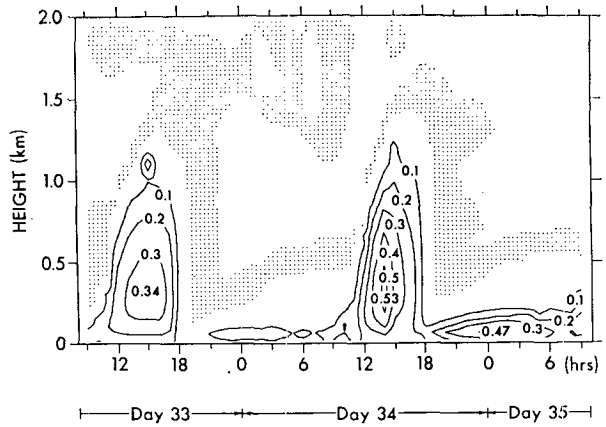

FIG. 18. The computed energy component $\overline{u^2}$, units $m^2 s^{-2}$. The areas stippled represent the regions where the values are between 10^{-3} and $10^{-2} m^2 s^{-2}$.

possibility of comparing the computed turbulence moments with data. Nevertheless the computed turbulence information is useful in enhancing understanding since we do believe the values are likely to be realistic.

The sum of the normal stresses (twice the turbulence kinetic energy), prognostically obtained by integrating Eq. (12), is presented in Fig. 11; its most striking feature is the strong contrast in magnitude and vertical extent between the daytime and nighttime profiles. The turbulence associated with large convective heating during the daytime diminishes almost completely after sunset. A second interesting feature is the maximum values located a few hundred meters above the surface especially when a strong upward heat flux exists. Figs. 12a and b show the various terms in the turbulent energy equation at 1400 and 1800 on Day 34. At 1400 the dissipation term and the buoyancy production term are nearly in balance except in the layer very close to the surface and at the top of the mixed layer so that Eq. (12) reduces to $q^3 \approx \Lambda_1 \beta g \overline{w\theta_v}$. Near the ground $\overline{w\theta_v}$

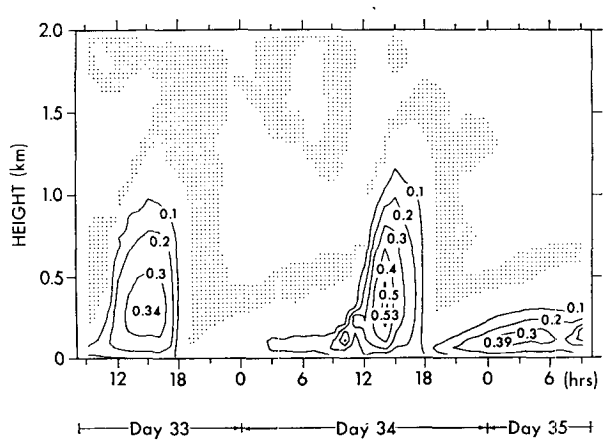

FIG. 19 The computed energy component $\overline{v^2}$.

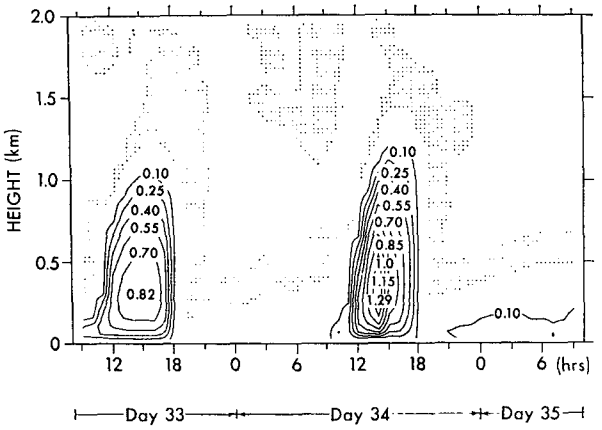

FIG. 20. The computed energy component $\overline{w^2}$.

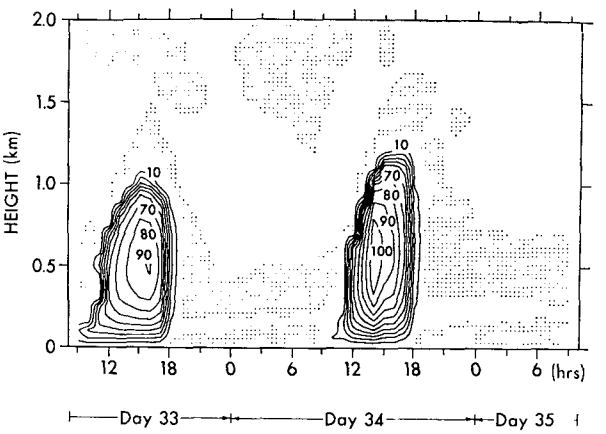

FIG. 22. Time and space variation of the computed eddy viscosity coefficient K_M, units $m^2\ s^{-1}$. The stippled areas correspond to the regions where K_M is between 0.01 and 0.5 $m^2\ s^{-1}$.

is almost constant, but $\Lambda_1 \sim kz$ so that the value for q^3 increases with height; then $\overline{w\theta_v}$ decreases whereas Λ_1 approaches a constant value.

At 1800 the dissipation term is more nearly in balance with the mechanical shear production term and the nighttime turbulence field is limited to the surface layer which is consistent with Fig. 11.

The computed results for $\overline{\theta_v^2}$ are shown in Fig. 13, whereas the terms in Eq. (13) have been plotted in Figs. 14a and b for 1400 and 1800 of Day 34. Note that the tendency and diffusion terms appear to be even less significant than was the case in the energy equation.

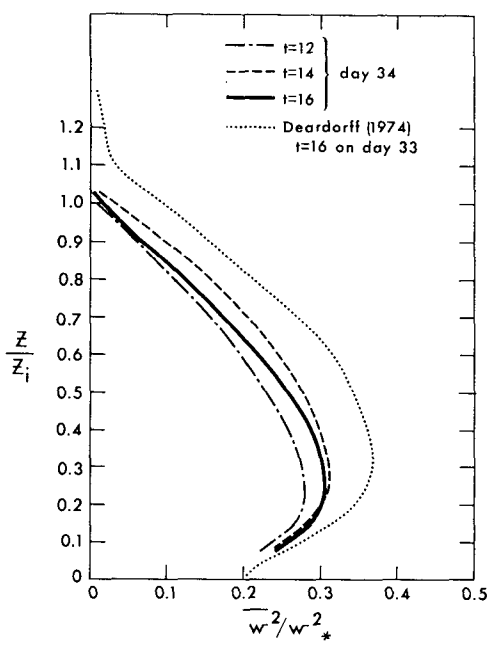

FIG. 21. Computed profiles of the dimensionless vertical velocity variance $\overline{w^2}$. The height is scaled by the depth of the mixed layer z_i and the variance by the convective velocity scale $w_* = (gH_0 z_i/\Theta_v)^{\frac{1}{3}}$ where H_0 represents the surface heat flux.

In contrast to the behavior of q^2 the temperature variance during the nighttime is comparable to daytime values within the surface layer. This is explained by the fact that the temperature variance equation has only a source term which is invariably positive whereas the energy equation has two source terms; during the night, the invariably positive shear production term is counteracted by a negative buoyancy production term.

The Reynolds stresses, $\overline{uw}$ and $\overline{vw}$, are shown in Figs. 15 and 16; they corroborate the notion of strong daytime convective mixing. This is also true of the turbulent heat flux, $\overline{w\theta_v}$, plotted in Fig. 17. Within the mixed layer, strong upward heat fluxes are observed during the daytime. However, regions of small downward heat flux exist above the mixed layer. Laboratory experiments by Deardorff *et al.* (1969) observed similar downward heat fluxes whose magnitudes are about 4% of those of the upward heat fluxes at the surface. The corresponding values in the present numerical model are about 2% at most. The three-dimensional nu-

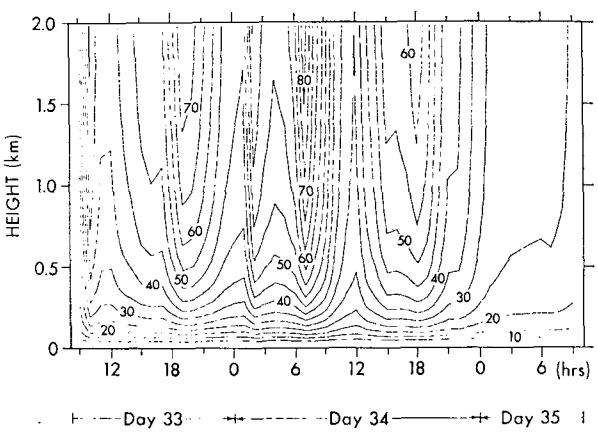

FIG. 23. Hourly profiles of the computed length scale l, units m.

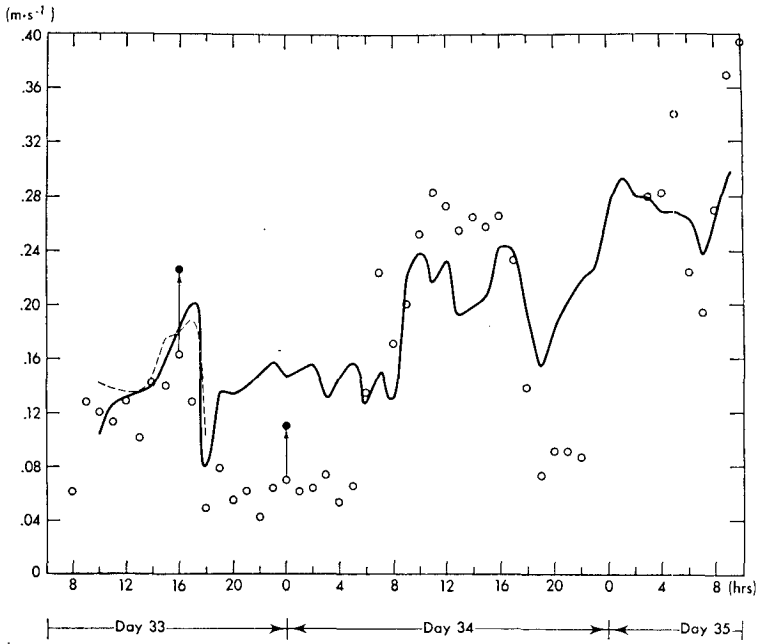

FIG. 24. Hourly variation of the computed and observed friction velocity: solid line, present study; dashed line, Deardorff (1974); open circles, observed ($z_0=0.12$ cm); filled circles, observed ($z_0=1$ cm).

merical model by Deardorff (1974b) produced values of 5–10% when simulating Day 33. The most important terms for the existence of the downward heat fluxes appear to be the turbulent energy diffusion terms (see again Fig. 12a) which maintain turbulence of small magnitude even in the strongly stable, stratified layer above the well-mixed layer; downward heat flux can be generated since the term $\overline{w^2}(\partial\Theta_v/\partial z)$ in Eq. (18c) becomes positive.

The three components of the wind variance are shown in Figs. 18–20. That the variances, $\overline{u^2}$ and $\overline{v^2}$, are similar to each other during the daytime may be anticipated from Eqs. (16a,b). In the free convection limit the vertical gradients of the horizontal wind components and, consequently, the mechanical shear production terms P_{xx} and P_{yy} in the turbulent energy equations become negligibly small as already seen in Fig. 12a. Thus $\overline{u^2}$ and $\overline{v^2}$ become equal as seen from Eqs. (16a,b).

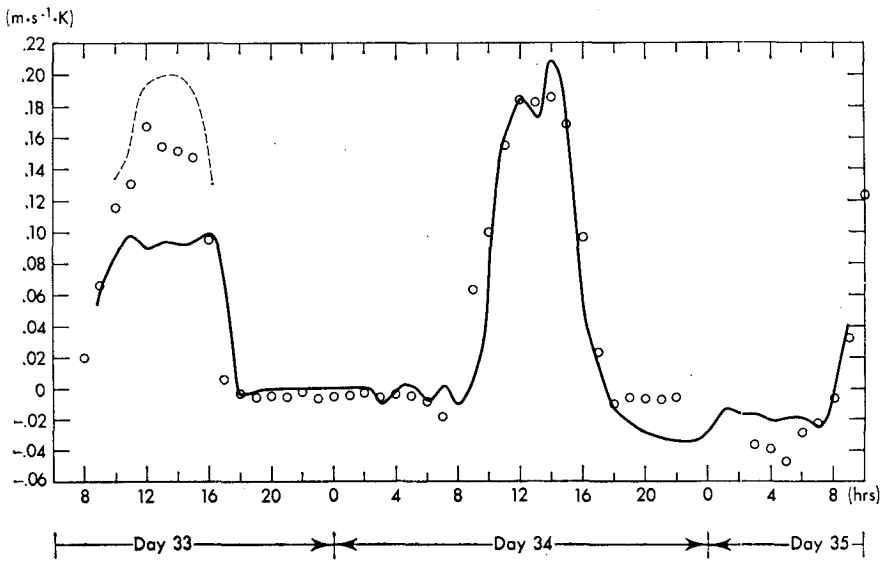

FIG. 25. Hourly variation of the computed and observed surface heat flux: solid line, present study; dashed line, Deardorff (1974); circles, observed.

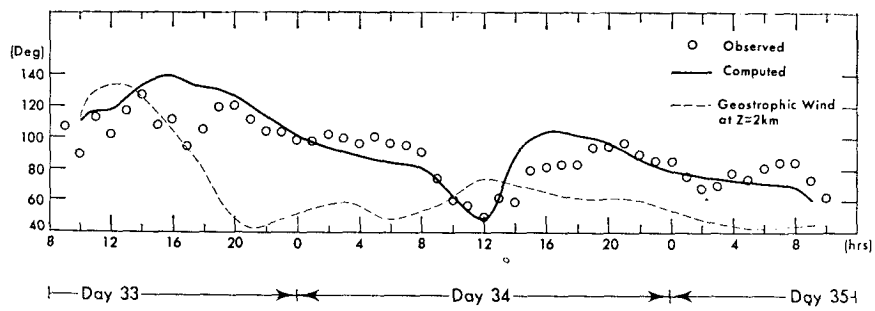

FIG. 26. Hourly variation of the computed and observed surface wind direction. Also included is the geostrophic wind direction at $z=2$ km.

Eq. (16c) also indicates why $\overline{w^2}$ is larger than $\overline{u}^2$ or $\overline{v}^2$. Note that large values of $\overline{w^2}$ are a primary ingredient in the exchange of mean velocity and temperature as seen in Eqs. (17b,c) and (18c).

Fig. 21 shows a comparison of the present values of $\overline{w^2}$ with those computed by Deardorff. The height is scaled by the depth z_i of the inversion layer, and the variance $\overline{w^2}$ is scaled by the convective velocity scale w_* defined as

$$w_* \equiv \left(\frac{g}{\Theta_v} H_0 z_i\right)^{\frac{1}{3}},$$

where H_0 represents the surface heat flux.

The computed eddy viscosity coefficient is shown in Fig. 22. Near the surface K_M is proportional to $ku_\tau z$; it increases to a maximum value somewhere around 500 m above the surface and then decreases. The eddy viscosity coefficients during the nighttime are small (<2 m^2 s^{-1}).

The length scale l governed by Eqs. (28a,b) is given by Fig. 23.

c. *Surface fluxes, wind direction and atmospheric warming rate*

Thus far we have utilized velocity data which are the average of five measuring stations; the lowest height for these average velocities was 50 m. However, the Wangara data set included velocity measurements at $z=0.5$ m at the center station from which we have computed the friction velocity by matching this near-surface wind to similarity wind profiles[4] (Businger *et al.*, 1971; Paulson, 1970). An inconsistency emerges here because the average reported roughness was $z_0 \sim 1$ cm (the value used in the calculations), whereas the reported best estimate of roughness at the center station was $z_0=0.12$ cm. Fig. 24 shows the comparison of data and calculations. The open circles are derived from the data when $z_0=0.12$ cm whereas the closed circles are obtained by using $z_0=1$ cm.

The computed surface heat flux $H_0=(-\overline{w\theta_v})_0$ is shown in Fig. 25. The observed values are reduced from the temperature difference at 1 and 2 m measured at the center station of the five-station array and an empirical temperature profile proposed by Businger *et al.* (1971).[5]

The computed and observed surface wind directions which are presented in Fig. 26 agree quite well. The observed wind directions were obtained not from wind components but from near-surface balloon trajectories. They vary almost 90° from a maxima value at 1500 on Day 33 to a minima value at 1200 on Day 34. For comparison, the geostrophic wind direction at 2 km as computed from the values in Figs. 5a and b is also plotted in Fig. 26. The difference between the surface and the geostrophic wind direction at 2 km is small during the daytime due to the strong mixing by turbulence, but it becomes larger during the nighttime.

The rate of warming or cooling due to heat transfer by turbulence, horizontal advection, vertical advection and radiation at 1400 and 1800 on Day 33 is shown in Fig. 27. The total heating rate at 1400 is nearly constant with height in the layer below 1000 m and is nearly equal to the divergence of the upward heat flux (Fig. 12a) except in the layer close to the ground where radiational warming is dominant. Since the gradient of the virtual potential temperature is small (Fig. 7) in the mixed layer, the magnitude of the term $W(\partial\Theta_v/\partial z)$ is also small although considerable subsidence is observed. Above 1000 m the large warming rate is associated with the subsidence and the positive virtual po-

[4] Thus

$$u_\tau = kU_m[\ln(z_m/z_0)-\psi_m]^{-1},$$

where

$$\psi_m \equiv \int_0^{\zeta_m} (1-\varphi_m)/\zeta d\zeta, \quad \varphi_m = \varphi_m(\zeta),$$

$\zeta=z/L$, $L\equiv u_\tau^3/(k\beta g H_0)$ and $z_m=0.5$ m. Empirical curve fits to the functions. $\varphi_m(\zeta)$ for stable and unstable flow have been suggested by Businger *et al.* (1971).

[5] Thus

$$H_0/u_\tau = 1.35k(\Theta_2-\Theta_1)[\ln(z_2/z_1)-\psi_h]^{-1},$$

where

$$\psi_h = \int_{\zeta_1}^{\zeta_2} (1-1.35\varphi_h)\zeta^{-1}d\zeta,$$

$z_1=1$ m and $z_2=2$ m. $\varphi_h(\zeta)$ for stable and unstable flow have been suggested by Businger *et al.* (1971).

TABLE 4. The variables corresponding to different sensitivity case studies.

Case	W	Variables (U_g, V_g)	α [Eq. (28b)]
Basic	data (Fig. 5)	data (Fig. 4a,b)	0.10
A	0	data (Fig. 4a,b)	0.10
B	data (Fig. 5)	$(-6,-6)$ m s^{-1}	0.10
C	0	$(-6,-6)$ m s^{-1}	0.10
D	same as the basic case		0.05

tential gradient seen in Fig. 7. The vertical gradient of the virtual potential temperature decreased from 9×10^{-3} K m^{-1} between 1200–1600 m to 0.5×10^{-3} K m^{-1} above 1800 m so that the total warming rate of the atmosphere decreased sharply with height above 1800 m although the downward motion was still substantial. The cooling rate due to radiation in the upper atmosphere is nearly constant at 0.5×10^{-3} K min^{-1} ($\sim$0.7 K day^{-1}).

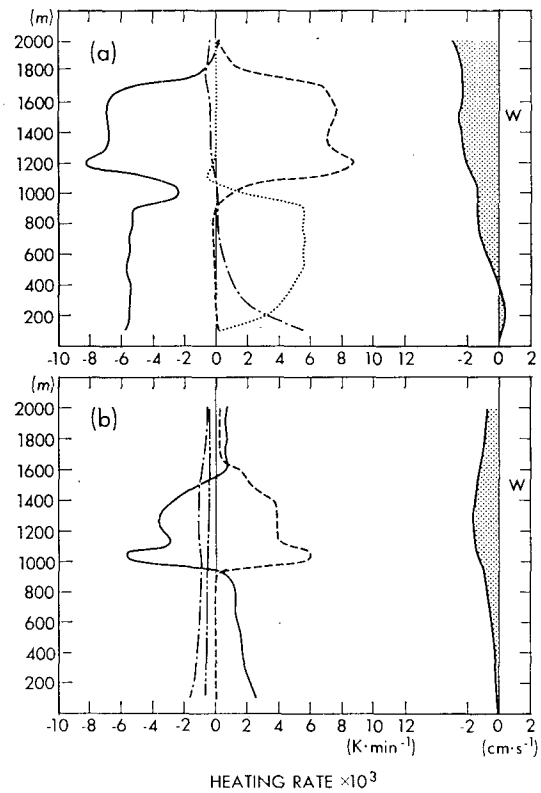

FIG. 27. Vertical profiles of the terms in the mean thermal energy equation: —— $-\partial\Theta_v/\partial t$, ····· $\partial(-\overline{w\theta_v})/\partial t$, – – – – $W(\partial\Theta_v/\partial z)$, —··— $-U(\partial\Theta_v/\partial x)-V(\partial\Theta_v/\partial y)$, —·—·— σ_r. Also included are the vertical profiles of the mean vertical wind. (a) 1400 Day 33, (horizontal advection was negligible); (b) 1800 Day 33 (heat flux divergence was negligible).

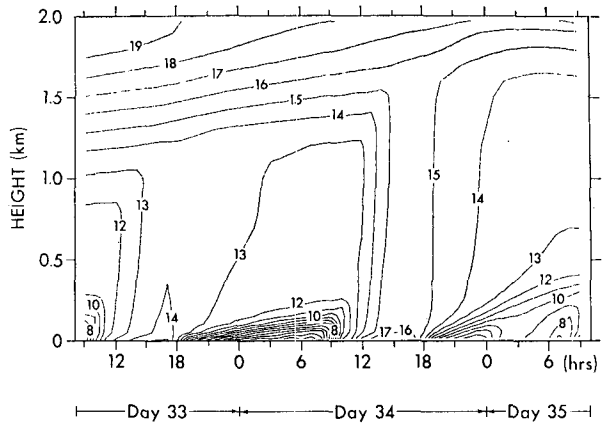

FIG. 28. Time and space variation of the computed mean virtual potential temperature when mean vertical winds are set equal to zero (Case A). The values indicate (Θ_v-273) in units of degrees K.

At 1800 the surface temperature began decreasing, and cooling due to radiation is found to be the dominant factor except in the 500 m deep layer just above the daytime well mixed layer (Fig. 27b). Here the atmosphere is still heated by the subsidence of warmer air from the upper layer. On the other hand, as seen from Fig. 6, subsequent upward vertical winds appear to prevent the temperature increasing indefinitely in this layer.

6. Sensitivity studies

Four additional numerical experiments have been designed to assay the sensitivity of the results if data on the mean vertical winds and/or the thermal winds were not available. The four cases are identified in Table 4. The basic case, discussed previously, utilizes the observed values for both the thermal wind and the mean vertical wind. To assess the effect of vertical wind we set $W=0$ for Case A. Case B assumes constant geostrophic wind components, $U_g=V_g=-6$ m s^{-1}, determined from Fig. 10 as the average value over the entire period of 48 h at 2 km above the surface. Therefore, a comparison of the Case B results, with those of the basic case, should indicate the importance of the thermal wind. In Case C, both the constant geostrophic winds and zero mean vertical winds are stipulated. Case D is added to assay the sensitivity of the results if the parameter α in the length scale equation (28b) is halved to 0.05.

The virtual potential temperature computed in Case A is exhibited in Fig. 28. The constant temperature contours are much smoother than those of the basic case in Fig. 7. Above the mixed layer, temperatures are uniformly decreased with time by cooling due to the horizontal advection and radiation. Although the accuracy of the measured vertical winds are suspect, their inclusion in the basic case evidently improved agreement with data. The computed mean winds (not

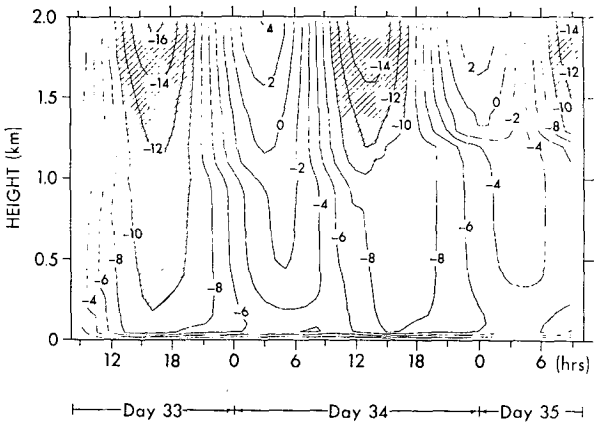

FIG. 29. Time and space variation of the computed eastward mean wind component (m s^{-1}) when constant geostrophic winds of $(U_g,V_g)=(-6,-6)$ m s^{-1} are assumed (case B).

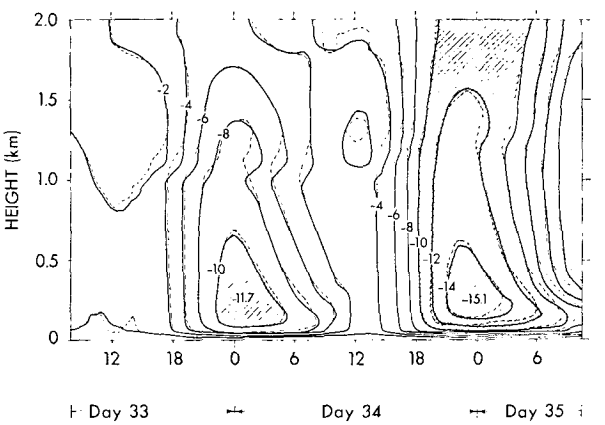

FIG. 31. As in Fig. 30 except for the eastward mean wind component U, units m s^{-1}.

shown) were not significantly different from the corresponding results for the basic case.

Fig. 29 shows the eastward wind component obtained in Case B which yields considerably poorer simulations in comparison with the basic case (see Fig. 8). However, the virtual potential temperature computed by Case B (not shown) compared fairly well with observation.

Case C, where $W=0$ and the geostrophic winds are constant, as expected, gave the poorest simulation among the four cases discussed above; these results have not been included here.

In paper A, the parameter $\alpha=0.10$ in the expression for the length scale l [Eqs. (28a,b)] was determined such that the height of a neutral, steady Ekman layer was about 0.30 u_τ/f. This value and possibly Eqs. (28a,b) itself are suspect. Thus, an additional numerical experiment was conducted under the same conditions as in the basic case but with the parameter α reduced by one-half. The computed mean velocity U and the virtual potential temperature, Θ_v are shown in Figs. 30 and 31 for $\alpha=0.05$ and 0.10. As seen from the figures, U and Θ_v are surprisingly insensitive to the change of α. Figs. 32a–c show the comparisons of the computed turbulent heat flux, Reynolds stress and the length scales for $\alpha=0.10$ and 0.5 at 1400 on Day 34. The surface heat flux and Reynolds stress are reduced by 20% and 5%, respectively.

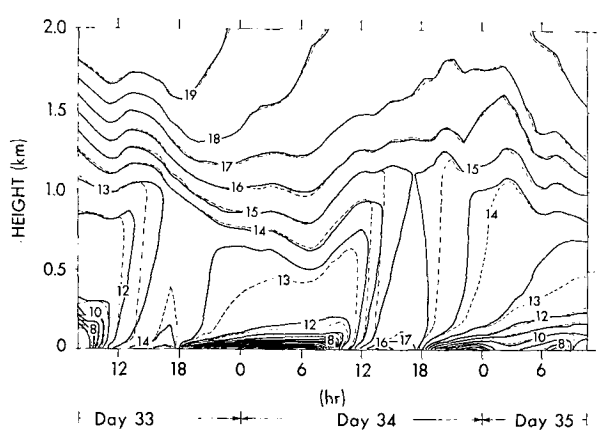

FIG. 30. Time and space variation of the computed mean virtual potential temperature with the parameter $\alpha=0.05$ in the length scale expression (28b). The results of the basic case ($\alpha=0.10$) are shown by the dashed lines. The values indicate (Θ_v-273) in units of degrees K.

7. Summary and conclusions

A numerical model is utilized to simulate the Wangara field experiment (Clarke *et al.*, 1971) for a period of 48 h from Day 33 through Day 35. The model requires the solution of two partial differential equations for the total turbulent kinetic energy and temperature variance in addition to differential equations for mean velocity and temperature. The remaining turbulent moments are obtained by simultaneously solving a set of algebraic equations. The simulation incorporates observed values for the thermal wind and mean vertical wind. The computed wind and virtual potential temperature exhibited qualitative and quantitative agreements with the observed values. Computed nocturnal low-level jets are of the right magnitude and location in comparison with the observations. A strong temperature inversion layer right above the well-mixed layer is successfully reproduced.

The computed turbulence moments indicate that the turbulence penetrates to about 1600 m above the ground during the daytime, diminishes very quickly as the sun sets, and is negligible during the nighttime.

Fig. 33 summarizes these events where we have differentiated a "mixing" layer of high turbulence intensity where mixing is active from a "mixed" layer of low turbulence intensity. The mixing or mixed layer height is defined as the height at which the vertical gradient of the virtual potential temperature abruptly

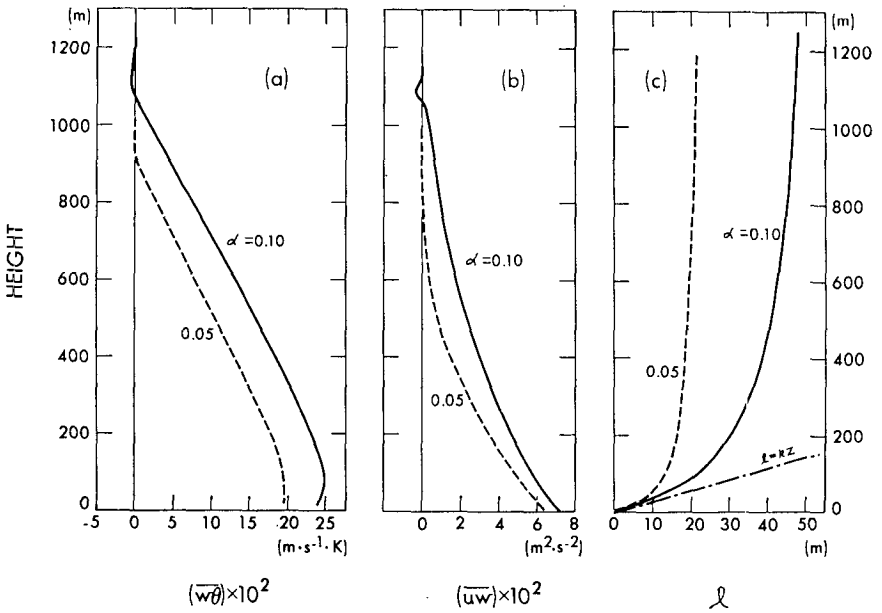

FIG. 32. Computed vertical profiles of turbulent heat flux (a), Reynolds stress $\overline{uw}$ (b), and length scale l (c), when $\alpha=0.05$ in Eq. (28b). The corresponding values obtained by the basic case ($\alpha=0.10$) are indicated by the dashed curves.

increases from nearly zero to a large value. The observed boundary layer depth in Fig. 33 is about 300 m higher than the computed one. If mean vertical wind were set to zero then the computed depth during the day would, on the average, agree better with the depth observed although the smaller scale variations in the computed boundary layer height would be less consistent with observation. Nevertheless, discrepancies between the observed and computed mixed layer heights could be attributed partially to the relatively large

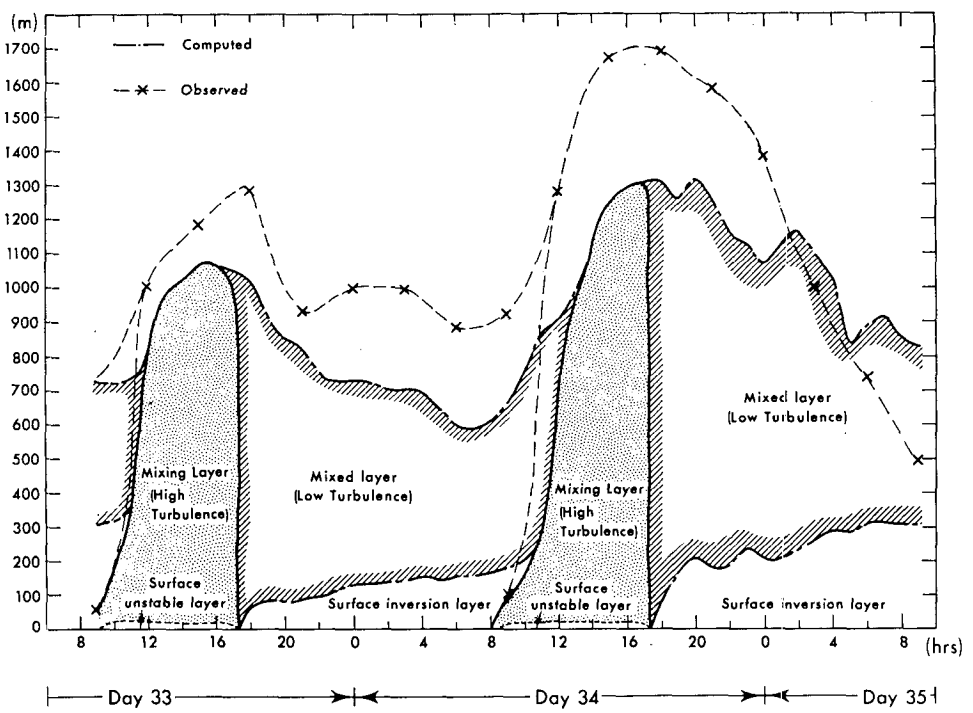

FIG. 33. Time evolution of the computed (basic case) and observed mixed layer height.

uncertainties in the observed values of the mean vertical wind.

Conventionally, the PBL height in a neutral atmosphere is thought to be proportional to u_τ/f. On the average, we find that a height of $0.3\,u_\tau/f$ is about right although, generally, this would be a poor estimate at any given time.

The expression for the length scale adopted in the present numerical model seems adequate although the mean velocity and temperature are found to be insensitive to a change of the parameter α in Eq. (28b) from 0.10 to 0.05. The computed turbulence moments are somewhat more strongly affected. Therefore, the optimum value for α must be determined from more complete comparisons of computed and observed profiles of the various turbulence moments.

Sensitivity studies indicate that the virtual potential temperature during the nighttime at 1000 m above the ground are about 3 K cooler if the mean vertical wind is set to zero. A model with constant geostrophic wind ($U_g=V_g=-6$ m s^{-1}) gave a poor simulation of the mean winds. Thus, it is concluded that fairly accurate data on the thermal wind and the mean vertical wind are required to obtain realistic simulations for both mean winds and temperature. There is little doubt that the prediction of the velocity field would be improved if the velocity advection terms were also known.

APPENDIX

Water Vapor

1. The mean and turbulent flux equations

The equation for the conservation of the mean mixing ratio of water vapor is

$$\frac{\partial R}{\partial t}+\frac{\partial}{\partial x_k}(U_kR+\overline{u_kr})=\eta\nabla^2R, \tag{A1}$$

where η is the kinematic diffusivity for water vapor, and the overbars represent ensemble averages. The equation for the covariances, $\overline{u_ir}$ and $\overline{\theta_vr}$, are

$$\begin{aligned}&\frac{\partial}{\partial t}(\overline{u_ir})+U_k\frac{\partial}{\partial x_k}(\overline{u_ir})\\&=-\overline{u_iu_k}\frac{\partial R}{\partial x_k}-\overline{u_kr}\frac{\partial U_i}{\partial x_k}-\frac{\partial}{\partial x_k}(\overline{u_iu_kr})\\&\quad-\frac{\partial}{\partial x_i}(\overline{pr})+p\frac{\overline{\partial r}}{\partial x_i}+\beta g\overline{r\theta_v}-\epsilon_{ikl}f_k\overline{u_lr}\\&\quad-(\eta+\nu)\overline{\frac{\partial U_i}{\partial x_k}\frac{\partial r}{\partial x_k}}+\eta\frac{\partial}{\partial x_k}\overline{\left(u_i\frac{\partial r}{\partial x_k}\right)}+\nu\frac{\partial}{\partial x_k}\overline{\left(r\frac{\partial u_i}{\partial x_k}\right)}\end{aligned} \tag{A2}$$

and

$$\begin{aligned}&\frac{\partial}{\partial t}(\overline{\theta_vr})+U_k\frac{\partial}{\partial x_k}(\overline{\theta_vr})=-\overline{u_k\theta_v}\frac{\partial R}{\partial x_k}-\overline{u_kr}\frac{\partial\Theta_v}{\partial x_k}-\frac{\partial}{\partial x_k}(\overline{u_k\theta_vr})\\&\quad-(\eta+\alpha)\overline{\frac{\partial\theta_v}{\partial x_k}\frac{\partial r}{\partial x_k}}+\eta\frac{\partial}{\partial x_k}\overline{\left(\theta_v\frac{\partial r}{\partial x_k}\right)}+\alpha\frac{\partial}{\partial x_k}\overline{\left(r\frac{\partial\theta_v}{\partial x_k}\right)}.\end{aligned} \tag{A3}$$

The equation for the variance $\overline{r^2}$ is

$$\begin{aligned}&\frac{\partial}{\partial t}\overline{r^2}+U_k\frac{\partial}{\partial x_k}\overline{r^2}=-2\overline{u_kr}\frac{\partial R}{\partial x_k}-\frac{\partial}{\partial x_k}(\overline{u_kr^2})\\&\quad+\eta\frac{\partial^2\overline{r^2}}{\partial x_k^2}-2\eta\overline{\frac{\partial r}{\partial x_k}\frac{\partial r}{\partial x_k}}.\end{aligned} \tag{A4}$$

In a fashion similar to that described by Mellor (1973), we now model the terms of the pressure–water vapor (gradient) correlation, dissipation, and third moments as follows:

$$\overline{p\frac{\partial r}{\partial x_i}}=-\frac{q}{3l_2}\overline{u_ir} \tag{A5a}$$

$$\overline{pr}=0 \tag{A5b}$$

$$(\eta+\nu)\overline{\frac{\partial u_i}{\partial x_k}\frac{\partial r}{\partial x_k}}=0 \tag{A5c}$$

$$(\eta+\alpha)\overline{\frac{\partial\theta_v}{\partial x_k}\frac{\partial r}{\partial x_k}}=\frac{2q}{\Lambda_2}\overline{\theta_vr} \tag{A5d}$$

$$2\eta\overline{\frac{\partial r}{\partial x_k}\frac{\partial r}{\partial x_k}}=\frac{2q}{\Lambda_2}\overline{r^2} \tag{A5e}$$

$$\overline{u_iu_kr}=-q\lambda_2\left(\frac{\partial\overline{u_kr}}{\partial x_i}+\frac{\partial\overline{u_ir}}{\partial x_k}\right) \tag{A5f}$$

$$\overline{u_k\theta_vr}=-q\lambda_2\left(\frac{\partial}{\partial x_k}\overline{\theta_vr}\right) \tag{A5g}$$

$$\overline{u_kr^2}=-q\lambda_3\frac{\partial\overline{r^2}}{\partial x_k}. \tag{A5h}$$

Substituting (A5a)–(A5h) into Eqs. (A2)–(A4) we obtain

$$\begin{aligned}&D(\overline{u_ir})/Dt+f_k\epsilon_{ik}\overline{u_ir}\\&=\frac{\partial}{\partial x_k}\left[q\lambda_2\left(\frac{\partial}{\partial x_i}\overline{u_kr}+\frac{\partial}{\partial x_k}\overline{u_ir}\right)+\eta\overline{u_i\frac{\partial r}{\partial x_k}}+\nu\overline{r\frac{\partial u_i}{\partial x_k}}\right]\\&\quad-\overline{u_iu_k}\frac{\partial R}{\partial x_k}-\overline{u_kr}\frac{\partial U_i}{\partial x_k}+\delta_{3i}\beta g\overline{r\theta_v}-\frac{q}{3l_2}\overline{u_ir}\end{aligned} \tag{A6}$$

$$D(\overline{\theta_v r})/Dt=\frac{\partial}{\partial x_k}\left[q\lambda_2\frac{\partial\overline{\theta_v r}}{\partial x_k}+\eta\overline{\theta_v}\frac{\partial\overline{r}}{\partial x_k}+\alpha\overline{r}\frac{\partial\overline{\theta_v}}{\partial x_k}\right]$$
$$-\overline{u_k\theta_v}\frac{\partial R}{\partial x_k}-\overline{u_k r}\frac{\partial\Theta_v}{\partial x_k}-\frac{2q}{\Lambda_2}\overline{\theta_v r} \quad \text{(A7)}$$

$$D(\overline{r^2}/2)/Dt=\frac{\partial}{\partial x_k}\left[q\lambda_3\frac{\partial}{\partial x_k}\left(\frac{\overline{r^2}}{2}\right)+\eta\frac{\partial}{\partial x_k}\left(\frac{\overline{r^2}}{2}\right)\right]$$
$$-\overline{u_k r}\frac{\partial R}{\partial x_k}-\frac{q}{\Lambda_2}\overline{r^2}. \quad \text{(A8)}$$

The Level 3 model is formally obtained by neglecting the advection and diffusion terms in Eq. (A6). The Level 3 model is described in the text.

2. The Level 2 model for water vapor.

To simplify the water vapor calculation, since accuracy of prediction suffers, *a priori*, from the omission of advective terms, we have utilized only a Level 2 model. This is obtained by neglecting diffusion and tendency terms in (14) and (15). Then with the help of (19c) it is possible to obtain

$$-\overline{wr}\equiv K_w\frac{\partial R}{\partial z}, \quad K_w=\frac{3l_2q\left(\overline{qw^2}+\beta\frac{\Lambda_2}{2}\overline{w\theta_v}\right)}{q^2+\frac{3}{2}\beta g l_2\Lambda_2\frac{\partial\Theta_v}{\partial z}}. \quad \text{(A9)}$$

[It is noteworthy that eddy-transport coefficients for heat and water vapor become equal if the advection and diffusion terms in Eq. (13) for $\overline{\theta_v^2}$ are neglected, in which case $K_W=K_H\equiv-\overline{\omega\theta_v}/(\partial\Theta_v/\partial Z)$.] The boundary condition similar to (36) is applied at the surafce where Θ_v is replaced by R. The surface water vapor R_m is available at the screen height every three hours. The upper boundary condition is $\partial R/\partial Z=0$ at $Z=2000$ m.

3. Modification of turbulent fluxes due to water vapor

In Eq. (2b), we have defined the virtual potential temperature according to

$$\tilde{\Theta}_v\equiv\tilde{\Theta}(1+\delta\tilde{R}), \quad \delta=0.61, \quad \text{(A10)}$$

where the tildes indicate instantaneous values. As in the text we remove the tildes to indicate mean values and utilize lower case letters to indicate fluctuating values. Taking an average of (A10), after the instantaneous values are replaced by the mean and fluctuating part, we obtain

$$\Theta_v=\Theta(1+\delta R)+\delta\overline{\theta r}. \quad \text{(A11)}$$

Then θ_v is given by

$$\theta_v\equiv\tilde{\Theta}_v-\Theta_v=\delta\Theta r+\theta(1+\delta R)+\delta(\theta r)-\delta\overline{\theta r}. \quad \text{(A12)}$$

Multiplying every term by u_j and taking averages, we have

$$\overline{u_j\theta_v}\approx\delta\Theta\overline{u_j r}+(1+\delta R)\overline{u_j\theta}, \quad \text{(A13)}$$

where the third turbulent moment $\delta\overline{u_j\theta r}$ is neglected.

In a similar fashion

$$\overline{\theta_v r}\approx\delta\Theta\overline{r^2}+(1+\delta R)\overline{\theta r}, \quad \text{(A14)}$$
$$\overline{\theta_v^2}\approx\delta^2\Theta^2\overline{r^2}+\overline{\theta^2}(1+\delta R)^2+2(1+\delta R)\Theta\overline{\theta r}. \quad \text{(A15)}$$

Eqs. (A11)–(A15) furnish relations between the "absolute" values and the corresponding "virtual" values.

4. The water vapor calculations

Since the present model does not include advection or evaporation and condensation, Eq. (6) for the mixing ratio of water vapor cannot be expected to reproduce

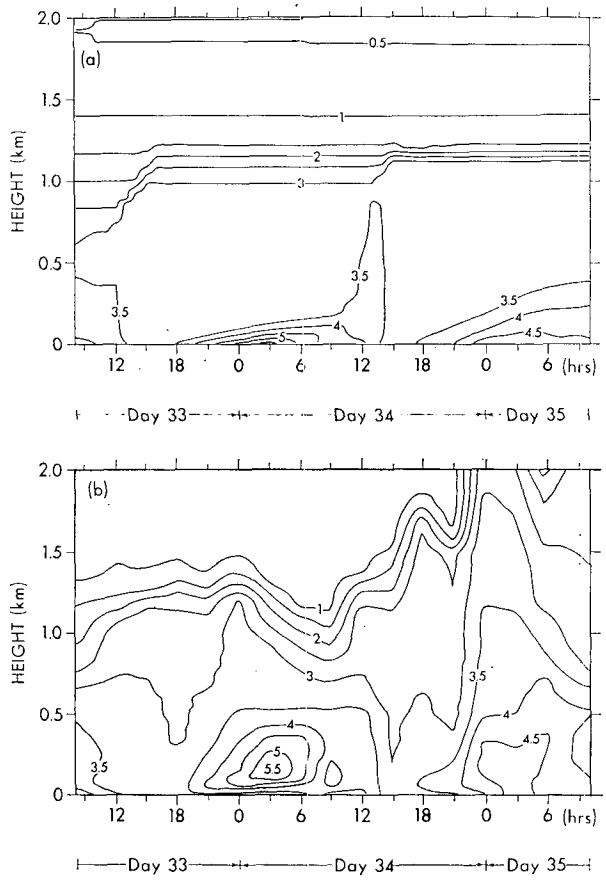

FIG. 34. Time and space variation of the computed (a) and observed (b) water vapor mixing ratio, units g kg^{-1}.

the observed profiles of the water vapor with accuracy nearly as well as for the winds and temperature. The computed and observed mixing ratio of water vapor, however, is presented in Figs. 34a and 34b. Profiles of the observed mixing ratio of water vapor show maximum values between 100 and 300 m above the ground during the nighttime cooling period. It is plausible that water vapor is condensed to liquid phase in the layer near the surface since the experiment was conducted during the winter season in Australia and the surface temperature decreased nearly to the freezing point.

Acknowledgments. The authors are grateful to Drs. S. Manabe and K. Miyakoda for carefully reading the manuscript and for valuable suggestions. Dr. S. Fels and Mr. D. Schwarzkopf have kindly provided us with a scheme to compute the longwave radiation for the atmosphere. Mr. R. Clarke has supplied us with the Wangara data on magnetic tape which were utilized to produce the contour line plots for comparison with the calculated results. The authors wish to thank Mmes. C. Longmuir and E. Olsen for typing the manuscript and Mr. P. Tunison for drafting the figures.

REFERENCES

Blackadar, A. K., 1957: Boundary layer wind maxima and their significance for the growth of nocturnal inversions. *Bull. Amer. Meteor. Soc.*, **38**, 283–290.

——, 1962: The vertical distribution of wind and turbulent exchange in neutral atmosphere. *J. Geophy. Res.*, **67**, 3095–3102.

Buajitti, K., and A. K. Blackadar, 1957: Theoretical studies of diurnal wind-structure variations in the planetary boundary layer. *Quart. J. Roy. Meteor. Soc.*, **83**, 486–500.

Businger, J. A., J. C. Wyngaard, Y. Izumi and E. F. Bradley, 1971: Flux profile relationships in the atmospheric surface layer. *J. Atmos. Sci.*, **28**, 181–189.

Clarke, R. H., 1974: Attempts to simulate the diurnal course of meteorological variables in the boundary layer. *Izv. Akad. Nauk SSSR, Fiz. Atmos. Okeana*, **10**, 600–612.

——, A. J. Dyer, R. R. Brook, D. G. Reid and A. J. Troup, 1971: The Wangara experiment: Boundary layer data. Tech. Paper 19, Div. Meteor. Phys. CSIRO, Australia.

Deardorff, J. W., 1974a: Three-dimensional numerical study of the height and mean structure of a heated planetary boundary layer. *Bound.-Layer Meteor.*, **1**, 81–106.

——, 1974b: Three-dimensional numerical study of turbulence in an entraining mixed layer. *Bound.-Layer Meteor.*, **1**, 199–226.

——, G. E. Willis and D. K. Lilly, 1969: Laboratory investigation of non-steady penetrative convection. *J. Fluid Mech.*, **35**, 7–31.

Donaldson, C. duP., 1973: Construction of a dynamic model of the production of atmospheric turbulence and the dispersal of atmospheric pollutants. *Workshop on Micrometeorology*, Amer. Meteor. Soc., 313–390.

Estoque, M., 1963: A numerical model of the atmospheric boundary layer. *J. Geophys. Res.*, **68**, 1103–1113.

Gamo, M., S. Yamamoto and O. Yokoyama, 1975: Distributions of the energy dissipation rate with height up to 1∼2 km. *Proc. Spring Meeting Meteor. Soc. Japan* (in Japanese), Tokyo, p. 27.

Hess, G. D., and R. H. Clarke, 1973: Time spectra and cross-spectra of kinetic energy in the planetary boundary layer. *Quart. J. Roy. Meteor. Soc.*, **99**, 130–153.

Hess, S. L., 1959: *Introduction to Theoretical Meteorology*. Holt, Rinehart and Winston, 362 pp.

Krishna, K., 1968: A numerical study of the diurnal variation of meteorological parameters in the planetary boundary layer: I Diurnal variation of winds. *Mon. Wea. Rev.*, **96**, 269–276.

Lenschow, D. H., 1970: Airplane measurements of planetary boundary layer structure. *J. Appl. Meteor.*, **9**, 874–884.

Lewellen, W. S., M. Teske and C. duP. Donaldson, 1974: Turbulence model of diurnal variations in the planetary boundary layer. *Proceed. 1974 Heat Transfer and Fluid Mechanics Institute*, L. R. Davis and R. E. Wilson, Eds., Stanford University Press, 301–319.

Lumley, J. L., and B. Khajeh-Nouri, 1974: Computational modeling of turbulent transport. *Advances in Geophysics*, Vol. 18A, Academic Press, 169–192.

Mellor, G. L., 1973: Analytic prediction of the properties of stratified planetary surface layers. *J. Atmos. Sci.*, **30**, 1061–1069.

——, and T. Yamada, 1974: A hierarchy of turbulence closure models for planetary boundary layer. *J. Atmos. Sci.*, **31**, 1791–1806.

Orlanski, I., B. B. Ross and L. J. Polinsky, 1974: Diurnal variation of the planetary boundary layer in a mesoscale model. *J. Atmos. Sci.*, **31**, 965–989.

Paegle, J., and G. E. Rasch, 1973: Three-dimensional characteristics of diurnally varying boundary-layer flows. *Mon. Wea. Rev.*, **101**, 746–756.

Paulson, C. A., 1970: The mathematical representation of wind speed and temperature profiles in the unstable atmospheric surface layer. *J. Appl. Meteor.*, **9**, 857–861.

Richtmyer, R. D., and K. W. Morton, 1967: *Difference Methods for Initial-Value Problems*. Interscience 405 pp.

Rotta, J. C., 1962: Turbulent boundary layers in incompressible flow. *Progress in Aeronautical Sciences*, Vol. 2, Pergamon Press, The Macmiillan Company, 1–219.

Sasamori, T., 1970: A numerical study of atmospheric and soil boundary layers. *J. Atmos. Sci.*, **27**, 1122–1137.

Telford, J. W., and J. Warner, 1964: Fluxes of heat and vapor in the lower atmosphere derived from aircraft observations. *J. Atmos. Sci.*, **21**, 539–548.

Wippermann, F., 1973: Numerical study on the effects controlling the low-level jet. *Beit. Phys. Atmos.*, **46**, 137–154.

Wyngaard, J. C. and O. R. Coté, 1974: The evolution of a convective planetary boundary layer—A higher-order-closure model study. *Bound.-Layer Meteor.*, **7**, 289–308.

Yamamoto, G., A. Shimanuki, M. Aida and N. Yasuda, 1973: Diurnal variation of wind and temperature fields in the Ekman layer. *J. Meteor. Soc. Japan.*, **51**, 377–387.